The Sloan Digital Sky Survey Reverberation Mapping Project: Initial C iv Lag Results from Four Years of Data

Item Type	Article
Authors	Grier, C. J.; Shen, Yue; Horne, Keith; Brandt, W. N.; Trump, J. R.; Hall, P. B.; Kinemuchi, K.; Starkey, David; Schneider, D. P.; Ho, Luis C.; Homayouni, Y.; Li, Jennifer I-Hsiu; McGreer, Ian D.; Peterson, B. M.; Bizyaev, Dmitry; Chen, Yuguang; Dawson, K. S.; Eftekharzadeh, Sarah; Guo, Yucheng; Jia, Siyao; Jiang, Linhua; Kneib, Jean-Paul; Li, Feng; Li, Zefeng; Nie, Jundan; Oravetz, Audrey; Oravetz, Daniel; Pan, Kaike; Petitjean, Patrick; Ponder, Kara A.; Rogerson, Jesse; Vivek, M.; Zhang, Tianmeng; Zou, Hu
Citation	C. J. Grier et al 2019 ApJ 887 38
DOI	10.3847/1538-4357/ab4ea5
Publisher	IOP PUBLISHING LTD
Journal	ASTROPHYSICAL JOURNAL
Rights	Copyright © 2019. The American Astronomical Society. All rights reserved.
Download date	27/08/2022 21:04:29
Item License	http://rightsstatements.org/vocab/InC/1.0/
Version	Final published version
Link to Item	http://hdl.handle.net/10150/636844

The Sloan Digital Sky Survey Reverberation Mapping Project: Initial C IV Lag Results from Four Years of Data

C. J. Grier[1,2,3], Yue Shen[4,5,28], Keith Horne[6], W. N. Brandt[1,2,7], J. R. Trump[8], P. B. Hall[9], K. Kinemuchi[10], David Starkey[4,6], D. P. Schneider[1,2], Luis C. Ho[11,12], Y. Homayouni[8], Jennifer I-Hsiu Li[4], Ian D. McGreer[3], B. M. Peterson[13,14,15], Dmitry Bizyaev[10,16], Yuguang Chen[17], K. S. Dawson[18], Sarah Eftekharzadeh[18], Yucheng Guo[12], Siyao Jia[19], Linhua Jiang[11], Jean-Paul Kneib[20,21], Feng Li[22], Zefeng Li[12], Jundan Nie[23], Audrey Oravetz[10], Daniel Oravetz[10], Kaike Pan[10], Patrick Petitjean[24], Kara A. Ponder[25], Jesse Rogerson[9,26], M. Vivek[1,2], Tianmeng Zhang[23,27], and Hu Zou[23]

[1] Department of Astronomy and Astrophysics, Eberly College of Science, The Pennsylvania State University, 525 Davey Laboratory, University Park, PA 16802, USA
[2] Institute for Gravitation & the Cosmos, The Pennsylvania State University, University Park, PA 16802, USA
[3] Steward Observatory, The University of Arizona, 933 North Cherry Avenue, Tucson, AZ 85721, USA
[4] Department of Astronomy, University of Illinois at Urbana-Champaign, Urbana, IL 61801, USA
[5] National Center for Supercomputing Applications, University of Illinois at Urbana-Champaign, Urbana, IL 61801, USA
[6] SUPA Physics and Astronomy, University of St. Andrews, Fife, KY16 9SS, UK
[7] Department of Physics, The Pennsylvania State University, University Park, PA 16802, USA
[8] Department of Physics, University of Connecticut, 2152 Hillside Road, Unit 3046, Storrs, CT 06269, USA
[9] Department of Physics and Astronomy, York University, Toronto, ON M3J 1P3, Canada
[10] Apache Point Observatory and New Mexico State University, P.O. Box 59, sunspot, NM 88349-0059, USA
[11] Kavli Institute for Astronomy and Astrophysics, Peking University, Beijing 100871, People's Republic of China
[12] Department of Astronomy, School of Physics, Peking University, Beijing 100871, People's Republic of China
[13] Department of Astronomy, The Ohio State University, 140 W 18th Avenue, Columbus, OH 43210, USA
[14] Center for Cosmology and AstroParticle Physics, The Ohio State University, 191 West Woodruff Avenue, Columbus, OH 43210, USA
[15] Space Telescope Science Institute, 3700 San Martin Drive, Baltimore, MD 21218, USA
[16] Sternberg Astronomical Institute, Moscow State University, Moscow, Russia
[17] California Institute of Technology, 1200 E California Blvd., MC 249-17, Pasadena, CA 91125, USA
[18] Department of Physics and Astronomy, University of Utah, 115 S. 1400 E., Salt Lake City, UT 84112, USA
[19] Department of Astronomy, University of California, Berkeley, CA 94720, USA
[20] Institute of Physics, Laboratory of Astrophysics, Ecole Polytechnique Fédérale de Lausanne (EPFL), Observatoire de Sauverny, 1290 Versoix, Switzerland
[21] Aix Marseille Université, CNRS, LAM (Laboratoire d'Astrophysique de Marseille) UMR 7326, F-13388, Marseille, France
[22] School of Mathematics and Physics, Changzhou University, Changzhou 213164, People's Republic of China
[23] Key Laboratory of Optical Astronomy, National Astronomical Observatories, Chinese Academy of Sciences, Beijing 100012, People's Republic of China
[24] Institut d'Astrophysique de Paris, Sorbonne Université and CNRS, 98bis Boulevard Arago, F-75014, Paris, France
[25] Berkeley Center for Cosmological Physics, University of California Berkeley, 341 Campbell Hall, Berkeley, CA 94720, USA
[26] Canada Aviation and Space Museum, 11 Aviation Parkway, Ottawa, ON, K1K 4Y5, Canada
[27] School of Astronomy and Space Science, University of Chinese Academy of Sciences, People's Republic of China

Abstract

We present reverberation-mapping (RM) lags and black hole mass measurements using the C IVλ1549 broad emission line from a sample of 348 quasars monitored as a part of the Sloan Digital Sky Survey RM Project. Our data span four years of spectroscopic and photometric monitoring for a total baseline of 1300 days, allowing us to measure lags up to ∼750 days in the observed frame (this corresponds to a rest-frame lag of ∼300 days in a quasar at $z = 1.5$ and ∼190 days at $z = 3$). We report significant time delays between the continuum and the C IVλ1549 emission line in 48 quasars, with an estimated false-positive detection rate of 10%. Our analysis of marginal lag measurements indicates that there are on the order of ∼100 additional lags that should be recoverable by adding more years of data from the program. We use our measurements to calculate black hole masses and fit an updated C IV radius–luminosity relationship. Our results significantly increase the sample of quasars with C IV RM results, with the quasars spanning two orders of magnitude in luminosity toward the high-luminosity end of the C IV radius–luminosity relation. In addition, these quasars are located at some of the highest redshifts ($z \approx 1.4$–2.8) of quasars with black hole masses measured with RM. This work constitutes the first large sample of C IV RM measurements in more than a dozen quasars, demonstrating the utility of multiobject RM campaigns.

Supporting material: figure sets, machine-readable tables

1. Introduction

Supermassive black holes (SMBHs) are nearly ubiquitous in massive galaxies across the universe, and their masses have been

shown to be correlated with a variety of properties of the galaxies in which they reside (e.g., Kormendy & Richstone 1995; Magorrian et al. 1998; Ferrarese & Merritt 2000; Gebhardt et al. 2000; Gültekin et al. 2009). As a consequence, theories and simulations regarding the evolution of galaxies must include SMBHs; explaining how SMBHs grew to their observed masses

---

[28] Alfred P. Sloan Research Fellow.

and how they are connected to their host galaxies is a critical component of galaxy evolution models. Accurate measurements of SMBH masses are therefore of paramount importance to successfully explaining the connection between galaxies and their SMBHs across the observable universe.

In nearby galaxies, black hole mass ($M_{\rm BH}$) measurements can be obtained from observations of stellar and gas dynamics near the center of the galaxy (e.g., McConnell & Ma 2013). However, this approach is currently infeasible for distant galaxies; to determine $M_{\rm BH}$ in galaxies beyond the local universe, we use active galactic nuclei (AGNs). Assuming that the broad emission lines observed in Type 1 AGNs are emitted by gas with motion that is dominated by the gravitational potential of the central SMBH, one can use this gas to obtain $M_{\rm BH}$ measurements. However, as the broad line-emitting regions (BLR) in most AGNs are too small to directly resolve with current technology (see Gravity Collaboration et al. (2018) for the only exception thus far), there are limited opportunities to learn about the size and structure of the BLR. Reverberation mapping (RM) is the primary technique employed for this (the other being gravitational microlensing; e.g., Morgan et al. 2010 and Mosquera et al. 2013).

RM uses the variability of AGNs to obtain BLR information: variations in the continuum flux (generally assumed to be emitted close to the SMBH) are echoed by gas in the BLR, with the signal from the BLR delayed by the light-travel time between the continuum-emitting source and the BLR gas (e.g., Blandford & McKee 1982; Peterson et al. 2004). Measuring this time delay determines the distance between these two regions, which yields a characteristic radius for the BLR, $R_{\rm BLR}$. This measurement can be combined with a characterization of the virial velocity of the gas, ΔV, which is assumed to be related to the width of the emission line, to yield a black hole mass:

$$M_{\rm BH} = \frac{f R_{\rm BLR} \Delta V^2}{G}, \qquad (1)$$

where f is a dimensionless factor that accounts for the geometry, orientation, and kinematics of the BLR.

In theory, RM measurements can be made using any suitably strong broad emission lines arising from gas that reverberates in response to the continuum and is in virial motion around the SMBH. Thus far, most ground-based efforts have been focused on the $H\beta$ emission line, which falls in the optical range in local AGNs, and additional strong optical lines such as $H\alpha$, $H\gamma$, and He IIλ4686. Attention has also been given to the C IVλ1549 and Mg IIλ2798 emission lines, which are often quite strong and lie within the optical range of many ground-based spectrographs for higher-redshift quasars. To date, on the order of 100 AGNs have RM measurements (e.g., Kaspi et al. 2000, 2005; Peterson et al. 2004; Bentz et al. 2009, 2010; Denney et al. 2010; Grier et al. 2012; Du et al. 2014, 2016a, 2016b; Barth et al. 2015; Hu et al. 2015; Grier et al. 2017; Lira et al. 2018).

RM measurements of local AGNs have established a tight correlation between $R_{\rm BLR}$ and the luminosity of the AGN (e.g., Kaspi et al. 2000, 2005; Bentz et al. 2013), with $R \propto \sqrt{L}$, consistent with basic photoionization expectations. This relation allows the estimation of $R_{\rm BLR}$ from a single spectrum, enabling $M_{\rm BH}$ estimates (hereafter referred to as single-epoch, or SE,

masses) for a large number of quasars for which RM campaigns are impractical (e.g., Shen et al. 2011). The current $H\beta$ $R_{\rm BLR}-L$ relationship is calibrated fairly well (Bentz et al. 2013), although there is a dearth of measurements at the high-luminosity end of the relation. The sample included in the most recent calibration of this relation is composed of ~40 nearby ($z < 0.3$), low-luminosity AGNs that may not be representative of the general AGN/quasar population. Recent studies by Du et al. (2016a) and Grier et al. (2017) find many objects below the measured relation, although the origin of this phenomenon is still currently under investigation and selection effects are likely relevant in some cases (e.g., Li et al. 2019; Fonseca Alvarez et al. 2019).

Many studies have focused on the C IVλ1549 emission line because it is one of the few strong lines in the ultraviolet (UV), making $M_{\rm BH}$ measurements in higher-redshift quasars feasible from the ground. The status of the C IV emission line with regards to measuring $M_{\rm BH}$ is complex: C IV frequently exhibits a blueshifted component reminiscent of outflows, and has been found to have significant nonreverberating components (e.g., Gaskell 1982; Korista et al. 1995; Richards et al. 2011; Denney 2012), though it has been suggested that many of the reported blueshifts are affected by incorrect redshift measurements (Denney et al. 2016a). In addition, these properties depend on luminosity—i.e., the blueshift is observed primarily in higher-luminosity quasars—and recent velocity-resolved RM results of the local Seyfert galaxy NGC 5548 (De Rosa et al. 2015; Horne et al. 2019, in preparation) show signatures indicative of a Keplerian disk with gas in virial motion, rather than evidence for outflowing gas. Possibly as a consequence of the above issue, differences have been reported between the full width at half maximum (FWHM) of C IV and the FWHM of $H\beta$ (Baskin & Laor 2005; Netzer et al. 2007; Shang et al. 2007; Shen & Kelly 2012; Trakhtenbrot & Netzer 2012; Shen 2013), with C IV sometimes showing narrower widths than $H\beta$. This has been interpreted as possible evidence against a simple radially stratified BLR that RM studies generally support (e.g., Peterson 1993; Korista et al. 1995). These issues have raised concerns over the suitability of C IV for SE $M_{\rm BH}$ estimates—though some studies suggest that data quality is the major issue, rather than C IV itself (e.g., Vestergaard & Peterson 2006; Denney 2012). Several corrections have been proposed to address these various issues and allow C IV to continue be used as an SE estimator (e.g., Assef et al. 2011; Denney 2012; Runnoe et al. 2013; Brotherton et al. 2015; Coatman et al. 2017). With or without these corrections, C IV has continued to be used to estimate $M_{\rm BH}$ in large numbers of sources (e.g., Shen et al. 2011).

Despite all of these potential issues, C IV can still be used for RM $M_{\rm BH}$ measurements, as RM methods make use of the root-mean-square (rms) line profile, which includes only the part of the C IV line that does reverberate. However, RM measurements of the C IV emission line are difficult to obtain. First, measurements in local galaxies require the use of space telescopes, as rest-frame C IV lies in the UV and is not accessible from the ground. Second, in higher-redshift, more luminous quasars, the expected observed lags are on the order of years (due to cosmological time dilation), making them impossible to measure in a single observing season and requiring long-term, logistically difficult observing campaigns. It is for these reasons that C IV RM measurements are far more scarce than $H\beta$ RM measurements. Thus far, there have

been only ∼15–18 C IV robust RM lag measurements that are used to calibrate the C IV $R_{BLR}-L$ relation (Peterson et al. 2004 and references therein; Peterson et al. 2005; Kaspi et al. 2007; Trevese et al. 2014; De Rosa et al. 2015; Lira et al. 2018; Hoormann et al. 2019), though there were some earlier reports of C IV lag detections of varying quality (e.g., Gaskell & Sparke 1986; Clavel et al. 1989; Koratkar & Gaskell 1989, 1991). The most recently measured $R_{BLR}-L$ relations for the C IV emission line (Lira et al. 2018; Hoormann et al. 2019) still contain relatively few measurements compared to the Hβ relation, and there are large ranges of luminosities along that relation for which there are no published measurements.

We have embarked on a large-scale, multiobject RM campaign called the Sloan Digital Sky Survey RM Project (SDSS-RM; Shen et al. 2015a), one of the major goals of which is to measure C IV lags in a large sample of quasars over a range of luminosities and redshifts. SDSS-RM began in 2014 as an ancillary program within the SDSS-III Baryon Oscillation Spectroscopic Survey (BOSS; Eisenstein et al. 2011; Dawson et al. 2013), and has continued to acquire spectra thereafter as a part of the SDSS-IV eBOSS program (Dawson et al. 2016; Blanton et al. 2017). Spectra of 849 quasars are obtained each observing season between January and July with the SDSS 2.5 m telescope (Gunn et al. 2006), and accompanying photometric data are acquired with the 3.6 m Canada–France–Hawaii Telescope (CFHT) and the Steward Observatory 2.3 m Bok telescope. Observations will continue to be taken through 2020. The main goals of the program are to obtain RM measurements using the Hβ, Mg II, and C IV emission lines for quasars over a wide range of redshifts; however, a wide variety of science topics can be (and have been) addressed with the rich data set provided by the SDSS-RM program, ranging from studies of quasar host galaxies, to broad absorption line (BAL) variability, to emission-line properties, to general quasar variability (e.g., Grier et al. 2015; Matsuoka et al. 2015; Shen et al. 2015b, 2016; Sun et al. 2015; Denney et al. 2016b; Yue et al. 2018; Hemler et al. 2019; Homayouni et al. 2019).

We here present C IV RM results from the SDSS-RM quasar sample using data taken during the first four years of the program (2014–2017). We present our quasar sample and the data used in our study in Section 2. In Section 3, we describe the methodology used for the various measurements. In Section 4, we discuss our results and their implications. We conclude in Section 5, with a summary of our main results. Throughout this article, we adopt a ΛCDM cosmology with $\Omega_\Lambda = 0.7$, $\Omega_M = 0.3$, and $h = 0.7$.

2. Data and Data Processing

2.1. The Quasar Sample

The parent sample of quasars consists of the 849 quasars monitored in the SDSS-RM field; details of this sample are provided by Shen et al. (2019b). We first restrict our sample to the 492 quasars with $z > 1.3$, i.e., quasars with observed-frame wavelength coverage of the C IV emission line in the BOSS spectra.

In many sources, however, the C IV emission line was not sufficiently variable to obtain RM measurements. Before performing our analysis, we thus first excluded sources whose C IV emission lines did not show significant variability over the span of our observations. To characterize the variability, we measured the C IV light curve variability signal-to-noise ratio (S/N) using the quantity S/N2, which is an output from the PrepSpec software (see Section 2.2 for a discussion of

PrepSpec). S/N2 is defined as $\sqrt{\chi^2 - \text{DOF}}$, where χ^2 is calculated against the average of the light curve flux (using the measurement uncertainties of the light curves σ_i), and DOF is the degrees of freedom, which is equal to the number of points in the light curve -1. Larger values of S/N2 indicate that the null-hypothesis model of no variability is a poor description of the emission-line light curve, while smaller values indicate that the light curve is consistent with zero variability. We require that the S/N2 of the C IV emission line is greater than 20 for a quasar to be included in our sample (this number was chosen based on visual inspection of the PrepSpec fits, light curves, and rms residual line profiles). This criterion produced a final sample of 348 quasars, with redshifts ranging from 1.35 to 4.32. Basic information on these quasars is provided in Table 1, and Figure 1 displays the distributions of redshift, i-mag, and luminosity of the quasars in our final sample.

2.2. Spectroscopic Data

We obtained the spectra used in this study during the first four years of observations for the SDSS-RM campaign (e.g., Shen et al. 2015a), which monitors 849 quasars with $i < 21.7$ at redshifts ranging from 0.1 to 4.5. The spectra were acquired with the BOSS spectrograph (Dawson et al. 2013; Smee et al. 2013), which covers a wavelength range of ∼3560–10400 Å. The spectrograph has a spectral resolution of $R \sim 2000$ and the data are binned to 69 km s^{-1} per pixel. We obtained a total of 68 epochs between 2014 January and 2017 July, with observations taken between January and July in each year only, leaving a gap of six months between observing seasons. The first year of SDSS-RM monitoring yielded 32 spectroscopic epochs and the additional three years of monitoring yielded 12 epochs each. Figure 2 displays the observing cadence for the observations.

The 2014 spectra were processed using the standard SDSS-III pipeline (version 5_7_1); data from the subsequent years were processed using the updated SDSS-IV eBOSS reduction pipeline (version 5_10_1). We then further processed all spectra using a custom flux-calibration scheme described by Shen et al. (2015a), which improves the spectrophotometric calibrations by using additional standard stars observed on the plate.

To further enhance the relative flux calibration of the data, we employed a custom procedure using software referred to as PrepSpec[29] (this code is described in detail by Shen et al. (2015a, 2016) and Horne et al. (2019, in preparation)). PrepSpec models the spectra using a variety of different components, and applies a time-dependent flux correction that is calculated by using the narrow emission lines (when present) as a calibrator. The correction assumes that there is no intrinsic variability in the fluxes of the narrow emission lines over the course of the campaign—some observations of long-term changes in narrow-line flux in local, low-luminosity sources have been reported (e.g., NGC 5548; Peterson et al. 2013), but simple luminosity scaling from NGC 5548 predicts narrow-line variability timescales of >30 rest-frame years in our quasars.

The PrepSpec model includes intrinsic variations in the continuum and broad emission lines, and the model is optimized to simultaneously fit all of the spectra of an object. In addition to the intrinsic variability of the continuum and emission lines,

---

[29] PrepSpec can be downloaded at http://star-www.st-andrews.ac.uk/~kdh1/lib/prepspec/prepspec.tar.gz.

Table 1
Quasar Sample Information

RMID	SDSS Identifier	R.A.[a] (deg) (J2000)	Decl.[a] (deg) (J2000)	z[b]	i mag[b]	$\log \lambda L_{\lambda 1350}$[b] (erg s^{-1})	$\log M_{\mathrm{BH,SE}}$[b,c] ($M_\odot$)	S/N2[d]
000	J141437.04+530422.7	213.6543	53.0730	1.464	20.837	$44.847 \pm 0.004^*$	$\cdots$	20.9
004	J141508.57+530019.7	213.7857	53.0055	2.767	21.254	45.377 ± 0.003	8.47 ± 0.02	20.3
006	J141401.85+530058.5	213.5077	53.0163	1.517	21.134	$44.996 \pm 0.002^*$	$\cdots$	29.8
011	J141534.20+525743.2	213.8925	52.9620	2.053	20.174	45.649 ± 0.001	9.09 ± 0.01	42.4
012	J141355.72+531202.3	213.4822	53.2006	1.585	21.499	$44.740 \pm 0.004^*$	$\cdots$	30.7
013	J141502.82+525401.2	213.7618	52.9003	1.850	21.201	44.915 ± 0.005	8.15 ± 0.02	20.6
019	J141529.69+525205.4	213.8737	52.8682	1.918	20.117	45.422 ± 0.001	8.68 ± 0.03	26.4
024	J141526.06+531941.7	213.8586	53.3283	1.552	21.483	$44.903 \pm 0.002^*$	$\cdots$	22.7
025	J141607.83+531535.0	214.0327	53.2597	1.816	21.365	45.234 ± 0.002	8.93 ± 0.01	50.4
028	J141543.08+525056.9	213.9295	52.8491	1.392	19.087	$45.786 \pm 0.001^*$	$\cdots$	48.6
031	J141640.89+530657.4	214.1704	53.1160	1.907	19.675	45.967 ± 0.001	9.04 ± 0.01	53.9
032	J141313.52+525550.2	213.3064	52.9306	1.715	20.341	44.492 ± 0.021	7.60 ± 0.03	79.5
034	J141254.00+530814.6	213.2250	53.1374	1.825	19.847	45.589 ± 0.001	8.71 ± 0.02	30.2
035	J141549.95+532005.5	213.9581	53.3349	1.803	20.310	45.502 ± 0.002	8.76 ± 0.02	42.7
036	J141420.55+532216.6	213.5856	53.3713	2.216	19.447	45.909 ± 0.001	9.11 ± 0.01	28.7
038	J141635.77+525649.3	214.1491	52.9470	1.383	18.757	$45.789 \pm 0.001^*$	$\cdots$	23.3
039	J141607.12+531904.8	214.0297	53.3180	3.041	19.769	45.619 ± 0.003	8.48 ± 0.07	71.9
041	J141643.78+525823.9	214.1824	52.9733	1.852	19.097	45.396 ± 0.002	9.05 ± 0.01	57.5
045	J141501.31+532438.5	213.7555	53.4107	3.060	20.295	45.974 ± 0.001	8.68 ± 0.02	22.0
049	J141416.10+524435.2	213.5671	52.7431	1.652	21.019	$45.285 \pm 0.001^*$	$\cdots$	20.2
051	J141352.16+532434.8	213.4673	53.4097	2.017	19.788	45.709 ± 0.001	9.00 ± 0.01	56.4
052	J141250.39+531719.6	213.2100	53.2888	2.305	20.701	45.499 ± 0.002	8.30 ± 0.02	26.9
055	J141627.75+524813.9	214.1157	52.8039	1.534	21.396	$44.895 \pm 0.003^*$	$\cdots$	36.6
057	J141721.81+530454.3	214.3409	53.0818	1.930	20.486	45.393 ± 0.003	8.33 ± 0.02	59.8
058	J141229.66+531431.7	213.1236	53.2422	2.300	21.381	45.353 ± 0.002	8.63 ± 0.01	30.5
059	J141721.28+530210.5	214.3387	53.0363	1.891	19.269	45.887 ± 0.001	8.90 ± 0.01	47.3
063	J141233.79+525240.0	213.1408	52.8778	1.537	20.899	$44.631 \pm 0.004^*$	$\cdots$	22.1
064	J141641.41+532147.1	214.1726	53.3631	2.216	20.768	45.390 ± 0.001	8.42 ± 0.05	36.4
065	J141357.11+524229.9	213.4880	52.7083	2.785	21.472	45.431 ± 0.003	8.65 ± 0.04	21.9
066	J141524.43+532832.7	213.8518	53.4758	2.148	21.295	45.173 ± 0.003	8.63 ± 0.04	49.8
069	J141408.56+524038.7	213.5357	52.6774	2.793	20.458	45.726 ± 0.001	8.53 ± 0.02	29.6
071	J141551.33+524119.9	213.9639	52.6889	1.693	20.721	45.354 ± 0.002	8.73 ± 0.01	34.8
072	J141658.42+524806.3	214.2434	52.8018	1.962	20.615	45.469 ± 0.001	8.99 ± 0.02	22.2
075	J141217.02+525127.4	213.0710	52.8576	2.655	19.596	46.059 ± 0.001	9.60 ± 0.01	23.7
076	J141331.06+532858.6	213.3794	53.4830	1.745	20.537	45.281 ± 0.002	8.75 ± 0.01	45.2
079	J141743.33+531145.6	214.4305	53.1960	2.059	20.851	45.384 ± 0.002	8.41 ± 0.02	21.6
080	J141224.60+532150.3	213.1025	53.3640	1.503	21.434	$44.720 \pm 0.005^*$	$\cdots$	33.6
081	J141527.96+523746.9	213.8665	52.6297	1.586	19.786	$45.557 \pm 0.001^*$	$\cdots$	39.4
086	J141756.95+525956.7	214.4873	52.9991	1.542	21.035	$44.893 \pm 0.003^*$	$\cdots$	21.1
087	J141327.46+523851.8	213.3645	52.6477	3.157	19.862	46.083 ± 0.001	8.76 ± 0.01	22.7
092	J141134.18+530005.1	212.8924	53.0014	1.357	20.155	$45.131 \pm 0.002^*$	$\cdots$	23.5
095	J141219.47+532457.4	213.0811	53.4160	2.316	21.457	45.202 ± 0.003	8.18 ± 0.01	24.5
097	J141340.50+523618.4	213.4188	52.6051	2.434	21.315	45.130 ± 0.003	8.21 ± 0.01	44.3
098	J141416.34+533508.3	213.5681	53.5857	2.454	21.254	44.816 ± 0.008	8.06 ± 0.02	60.8
107	J141817.46+531116.8	214.5728	53.1880	2.234	20.436	45.437 ± 0.002	8.48 ± 0.01	45.3
108	J141226.77+524120.3	213.1116	52.6890	2.193	21.013	45.375 ± 0.002	8.70 ± 0.02	22.7
110	J141807.73+531754.0	214.5322	53.2983	2.281	20.671	45.439 ± 0.002	8.90 ± 0.01	23.4
112	J141132.56+525111.5	212.8857	52.8532	1.397	19.793	$44.956 \pm 0.003^*$	$\cdots$	40.1
116	J141432.46+523154.5	213.6353	52.5318	1.878	19.681	45.652 ± 0.001	8.90 ± 0.03	34.5
117	J141829.50+530207.8	214.6229	53.0355	2.007	20.227	45.714 ± 0.001	9.15 ± 0.01	27.3
119	J141135.55+524814.4	212.8982	52.8040	2.729	20.048	46.060 ± 0.001	8.53 ± 0.01	39.6
124	J141708.46+533253.6	214.2853	53.5482	2.015	19.854	45.653 ± 0.001	8.86 ± 0.01	30.6
128	J141103.17+531551.3	212.7632	53.2643	1.862	20.012	45.359 ± 0.002	8.68 ± 0.05	24.2
130	J141735.33+523851.4	214.3972	52.6476	1.960	20.036	45.534 ± 0.001	8.39 ± 0.03	39.6
137	J141112.59+532254.5	212.8025	53.3818	3.266	21.129	45.709 ± 0.003	8.46 ± 0.02	24.8
142	J141803.36+524127.7	214.5140	52.6910	1.685	20.024	45.480 ± 0.003	8.96 ± 0.01	69.2
144	J141843.30+531920.8	214.6804	53.3225	2.300	20.685	45.516 ± 0.001	8.90 ± 0.01	38.9
145	J141818.45+524356.0	214.5769	52.7322	2.137	21.592	45.113 ± 0.004	8.76 ± 0.03	63.2
149	J141903.89+530855.4	214.7662	53.1487	1.623	21.310	$44.796 \pm 0.003^*$	$\cdots$	28.5
150	J141252.32+523046.1	213.2180	52.5128	1.493	20.765	$45.057 \pm 0.002^*$	$\cdots$	22.4
153	J141101.15+532327.7	212.7548	53.3910	2.753	19.761	45.831 ± 0.001	9.01 ± 0.01	28.9
154	J141704.00+533807.4	214.2667	53.6354	2.499	21.613	45.205 ± 0.004	8.79 ± 0.01	51.5

Table 1
(Continued)

RMID	SDSS Identifier	R.A.[a] (deg) (J2000)	Decl.[a] (deg) (J2000)	z[b]	i mag[b]	$\log \lambda L_{\lambda 1350}$[b] (erg s^{-1})	$\log M_{\mathrm{BH,SE}}$[b,c] ($M_\odot$)	S/N2[d]
155	J141123.68+532845.7	212.8487	53.4794	1.657	19.650	$45.364 \pm 0.001^*$	⋯	46.8
156	J141334.20+534222.0	213.3925	53.7061	1.660	20.388	$45.148 \pm 0.002^*$	⋯	25.5
157	J141045.53+531943.5	212.6897	53.3288	1.383	19.958	$45.125 \pm 0.002^*$	⋯	37.5
158	J141754.72+533254.8	214.4780	53.5486	1.478	20.378	$44.999 \pm 0.004^*$	⋯	31.9
159	J141446.74+522523.7	213.6948	52.4233	1.587	19.451	$45.740 \pm 0.001^*$	⋯	50.7
161	J141048.88+524839.8	212.7037	52.8111	2.067	20.669	45.491 ± 0.001	8.32 ± 0.04	54.2
164	J141655.72+534012.1	214.2322	53.6700	1.907	21.658	44.985 ± 0.005	7.65 ± 0.02	38.4
172	J141020.78+531316.8	212.5866	53.2213	3.207	18.193	46.792 ± 0.000	9.54 ± 0.00	33.0
176	J141801.94+523514.9	214.5081	52.5875	1.497	19.425	$45.473 \pm 0.001^*$	⋯	26.2
178	J141852.89+532533.4	214.7204	53.4260	1.947	20.614	45.585 ± 0.001	8.75 ± 0.02	35.1
179	J141357.48+534612.8	213.4895	53.7702	2.265	21.155	45.152 ± 0.003	8.37 ± 0.07	23.6
180	J141007.73+530719.4	212.5322	53.1221	3.101	19.815	46.166 ± 0.001	9.23 ± 0.03	28.1
181	J141040.30+524523.1	212.6679	52.7564	1.675	21.392	44.545 ± 0.015	7.79 ± 0.04	35.6
182	J141121.05+523634.6	212.8377	52.6096	1.571	20.430	$45.253 \pm 0.001^*$	⋯	39.0
186	J141022.58+532034.5	212.5941	53.3429	1.393	21.589	$45.168 \pm 0.002^*$	⋯	40.5
190	J141005.94+531333.7	212.5248	53.2260	1.992	21.013	45.284 ± 0.003	8.30 ± 0.02	53.0
194	J141231.13+522632.0	213.1297	52.4422	1.560	20.778	$44.700 \pm 0.004^*$	⋯	27.4
196	J140957.62+530959.6	212.4901	53.1666	1.595	21.378	$44.775 \pm 0.004^*$	⋯	25.4
201	J141215.24+534312.1	213.0635	53.7200	1.812	18.375	46.240 ± 0.001	9.40 ± 0.01	61.2
202	J140958.54+525516.6	212.4940	52.9213	2.635	19.803	45.927 ± 0.001	8.61 ± 0.01	58.9
205	J141924.44+532315.5	214.8519	53.3877	2.940	19.318	46.002 ± 0.001	9.00 ± 0.02	51.1
207	J141738.54+534251.0	214.4106	53.7142	2.620	18.784	46.361 ± 1.000	⋯	33.0
208	J141943.58+525431.3	214.9316	52.9087	3.440	21.265	45.587 ± 0.003	8.18 ± 0.03	21.7
210	J141952.79+530204.2	214.9700	53.0345	1.903	20.922	45.346 ± 0.002	8.50 ± 0.01	25.9
213	J141418.23+535046.8	213.5760	53.8463	2.716	21.034	45.419 ± 0.002	8.65 ± 0.02	28.7
216	J141541.99+521921.7	213.9250	52.3227	2.036	21.615	45.396 ± 0.002	8.97 ± 0.01	28.0
217	J141000.68+532156.1	212.5029	53.3656	1.817	20.388	45.382 ± 0.002	8.67 ± 0.02	31.4
218	J141229.98+522323.6	213.1249	52.3899	2.102	20.900	45.402 ± 0.002	8.12 ± 0.06	26.9
220	J141918.07+524158.4	214.8253	52.6996	2.038	20.412	45.669 ± 0.001	8.81 ± 0.02	28.0
222	J141044.47+533407.0	212.6853	53.5686	2.009	21.355	45.081 ± 0.004	8.40 ± 0.01	59.8
225	J141920.23+532838.9	214.8343	53.4775	1.838	21.392	45.059 ± 0.004	8.10 ± 0.03	38.1
226	J141431.50+535154.6	213.6313	53.8652	2.915	20.804	45.396 ± 0.003	9.44 ± 0.44	26.4
227	J141816.24+522940.6	214.5677	52.4946	1.608	19.906	$45.541 \pm 0.001^*$	⋯	26.0
230	J141005.73+524342.2	212.5239	52.7284	2.003	18.776	45.732 ± 0.001	9.17 ± 0.04	30.1
231	J142005.59+530036.7	215.0233	53.0102	1.645	19.794	$45.736 \pm 0.001^*$	⋯	59.5
237	J141021.95+523813.2	212.5915	52.6370	2.392	19.600	45.866 ± 0.001	9.20 ± 0.01	51.6
238	J141750.37+534517.7	214.4599	53.7549	2.189	20.115	45.831 ± 0.001	8.92 ± 0.03	32.3
241	J141738.83+522333.0	214.4118	52.3925	2.155	20.522	45.271 ± 0.003	8.14 ± 0.03	55.0
242	J142010.48+531223.8	215.0437	53.2066	2.591	20.050	45.652 ± 0.002	9.16 ± 0.02	24.7
244	J140942.79+532219.3	212.4283	53.3720	1.759	20.575	44.627 ± 0.021	8.95 ± 0.12	33.1
245	J141347.68+521646.2	213.4487	52.2795	1.670	20.903	45.351 ± 0.004	9.22 ± 0.01	23.1
249	J141956.29+532402.6	214.9846	53.4007	1.717	21.002	44.984 ± 0.010	7.89 ± 0.06	45.6
251	J141554.32+535357.0	213.9763	53.8992	2.196	20.862	45.324 ± 0.002	8.43 ± 0.09	31.0
253	J141918.12+533453.3	214.8255	53.5815	1.817	19.903	45.470 ± 0.001	8.79 ± 0.01	27.2
256	J141334.12+535430.3	213.3922	53.9084	2.244	21.640	45.089 ± 0.003	8.27 ± 0.03	32.5
257	J140931.90+532302.2	212.3830	53.3840	2.419	19.541	45.782 ± 0.005	9.19 ± 0.04	20.6
259	J142025.58+531105.2	215.1066	53.1848	1.845	21.401	44.777 ± 0.010	8.74 ± 0.06	27.5
262	J141325.87+535440.6	213.3578	53.9113	3.170	20.826	46.007 ± 0.004	8.90 ± 0.01	23.9
264	J141214.19+535055.2	213.0591	53.8487	2.120	21.513	45.434 ± 0.002	8.72 ± 0.01	67.5
266	J141002.92+533334.4	212.5122	53.5596	2.392	21.277	45.582 ± 0.002	8.47 ± 0.01	25.2
269	J141929.90+533501.4	214.8746	53.5837	2.393	21.269	45.193 ± 0.003	8.13 ± 0.03	20.4
275	J140951.81+533133.7	212.4659	53.5260	1.577	20.154	$45.611 \pm 0.001^*$	⋯	118.5
279	J140945.82+523950.4	212.4409	52.6640	2.398	21.297	45.627 ± 0.001	8.61 ± 0.03	30.6
280	J141949.19+533207.7	214.9550	53.5355	1.366	19.494	$45.711 \pm 0.001^*$	⋯	40.5
282	J141938.71+523537.7	214.9113	52.5938	3.353	21.525	45.052 ± 0.008	8.40 ± 0.04	24.8
283	J141712.26+521655.8	214.3011	52.2822	1.847	20.524	45.715 ± 0.001	8.53 ± 0.02	32.6
284	J141927.35+533727.7	214.8640	53.6244	2.386	20.216	45.642 ± 0.001	9.05 ± 0.05	53.0
286	J142040.56+530740.7	215.1690	53.1280	1.751	20.772	44.904 ± 0.005	8.50 ± 0.03	30.1
293	J141923.06+533936.5	214.8461	53.6601	1.849	21.133	45.201 ± 0.002	8.59 ± 0.02	21.6
295	J141347.87+521204.9	213.4495	52.2014	2.352	20.800	45.605 ± 0.001	8.87 ± 0.01	47.7
298	J141155.56+521802.9	212.9815	52.3008	1.635	19.997	$45.596 \pm 0.001^*$	⋯	27.0
304	J140847.22+530235.2	212.1968	53.0431	1.492	20.606	$45.414 \pm 0.001^*$	⋯	36.9

Table 1
(Continued)

RMID	SDSS Identifier	R.A.[a] (deg) (J2000)	Decl.[a] (deg) (J2000)	z[b]	i mag[b]	log $\lambda L_{\lambda 1350}$[b] (erg s^{-1})	log $M_{\mathrm{BH,SE}}$[b,c] ($M_\odot$)	S/N2[d]
310	J141220.09+535513.2	213.0837	53.9204	2.770	20.561	45.717 ± 0.002	9.34 ± 0.02	28.8
312	J140942.41+523516.7	212.4267	52.5880	1.924	21.441	45.077 ± 0.004	8.86 ± 0.02	47.8
317	J141905.16+522527.6	214.7715	52.4244	1.602	19.677	45.520 ± 0.001*	⋯	45.1
318	J141248.18+521243.6	213.2008	52.2121	1.515	19.416	45.714 ± 0.001*	⋯	30.6
319	J141842.55+534828.8	214.6773	53.8080	2.337	21.345	45.296 ± 0.002	8.64 ± 0.02	22.0
321	J142043.67+532206.3	215.1820	53.3684	1.720	19.013	45.703 ± 0.001	8.55 ± 0.01	41.4
322	J141851.53+534748.0	214.7147	53.7967	2.028	21.629	44.780 ± 0.005	8.10 ± 0.03	30.8
327	J142015.64+523718.8	215.0652	52.6219	1.675	19.101	45.821 ± 0.001	8.88 ± 0.01	55.0
330	J141647.20+521115.2	214.1967	52.1876	2.156	18.497	46.453 ± 0.000	9.51 ± 0.00	55.1
332	J140843.68+524941.0	212.1820	52.8281	2.581	21.203	45.551 ± 0.002	8.15 ± 0.02	51.7
334	J141910.22+534707.1	214.7926	53.7853	2.375	20.323	45.716 ± 0.001	8.53 ± 0.03	58.2
335	J141932.07+522639.4	214.8837	52.4443	2.167	21.087	45.491 ± 0.002	8.56 ± 0.03	37.1
339	J142014.84+533609.0	215.0618	53.6025	2.010	20.004	45.743 ± 0.001	8.94 ± 0.01	24.0
342	J140822.40+530451.8	212.0934	53.0811	1.696	19.474	45.834 ± 0.001	9.11 ± 0.01	54.9
343	J141104.13+521755.4	212.7672	52.2987	2.895	19.148	46.253 ± 0.001	8.69 ± 0.01	45.4
344	J142113.25+531218.5	215.3052	53.2052	1.948	20.777	45.161 ± 0.003	8.66 ± 0.01	46.8
345	J141041.89+522020.4	212.6746	52.3390	3.550	21.279	45.647 ± 0.003	8.30 ± 0.04	26.1
346	J141843.67+535138.5	214.6820	53.8607	1.589	20.672	44.905 ± 0.003*	⋯	35.0
348	J142039.95+524014.9	215.1665	52.6708	1.676	19.756	45.367 ± 0.003	7.95 ± 0.08	31.6
349	J142005.04+533937.3	215.0210	53.6604	3.614	21.291	45.788 ± 0.002	8.52 ± 0.02	26.1
351	J141114.52+521611.0	212.8105	52.2697	1.717	20.790	44.788 ± 0.009	8.03 ± 0.04	44.2
353	J140851.64+524134.2	212.2152	52.6928	2.191	20.183	45.598 ± 0.001	8.69 ± 0.02	42.9
358	J140954.32+522528.5	212.4764	52.4246	1.906	20.159	45.268 ± 0.003	8.54 ± 0.04	86.1
359	J142117.99+525346.0	215.3250	52.8961	2.309	20.051	45.838 ± 0.001	9.02 ± 0.01	32.9
361	J142100.22+524342.3	215.2509	52.7284	1.617	19.459	45.576 ± 0.001*	⋯	42.9
362	J141730.52+521019.4	214.3772	52.1721	1.860	20.906	45.301 ± 0.003	8.91 ± 0.02	25.6
363	J142113.29+524929.9	215.3054	52.8250	2.635	19.000	46.497 ± 0.001	9.68 ± 0.01	24.6
366	J142041.26+533355.3	215.1719	53.5654	2.420	20.843	45.626 ± 0.001	8.95 ± 0.02	25.9
372	J141236.48+540152.1	213.1520	54.0311	1.745	20.246	45.616 ± 0.001	9.09 ± 0.01	63.0
379	J141138.20+535906.2	212.9092	53.9851	2.321	19.972	45.921 ± 0.001	8.66 ± 0.01	71.1
380	J140801.53+530500.7	212.0064	53.0836	1.969	20.415	45.527 ± 0.001	8.90 ± 0.02	29.7
381	J140827.41+532710.2	212.1142	53.4528	2.538	20.058	46.152 ± 0.001	8.77 ± 0.01	64.7
383	J142136.28+530113.7	215.4012	53.0205	4.288	21.048	45.853 ± 0.002	8.34 ± 0.03	22.1
386	J142050.74+533514.9	215.2114	53.5875	1.865	20.803	45.279 ± 0.002	8.39 ± 0.01	22.4
387	J141905.24+535354.1	214.7719	53.8984	2.426	19.977	45.687 ± 0.001	8.83 ± 0.02	51.9
389	J141839.03+521333.0	214.6627	52.2259	1.850	19.656	45.564 ± 0.002	8.97 ± 0.01	59.2
394	J140846.62+533613.5	212.1943	53.6038	1.966	21.160	44.905 ± 0.007	8.04 ± 0.04	25.6
396	J140751.37+531024.5	211.9641	53.1735	1.836	21.072	44.911 ± 0.005	8.70 ± 0.04	28.4
397	J142136.51+532014.2	215.4022	53.3373	2.017	21.497	45.068 ± 0.004	8.18 ± 0.02	34.0
401	J140957.28+535047.0	212.4887	53.8464	1.822	20.226	45.490 ± 0.003	8.55 ± 0.03	43.2
403	J140758.42+525058.2	211.9935	52.8495	1.612	20.444	44.940 ± 0.002*	⋯	32.6
405	J142109.48+523800.1	215.2895	52.6334	3.386	19.921	46.082 ± 0.001	8.81 ± 0.03	34.8
408	J141409.85+520137.2	213.5411	52.0270	1.734	19.630	45.708 ± 0.001	8.47 ± 0.09	49.4
409	J140916.98+522535.0	212.3208	52.4264	2.110	18.765	46.181 ± 0.001	9.05 ± 0.02	74.6
410	J140944.88+535002.7	212.4370	53.8341	1.819	20.773	45.579 ± 0.001	9.04 ± 0.01	41.5
411	J141252.35+540628.0	213.2181	54.1078	1.734	20.888	44.887 ± 0.007	8.29 ± 0.02	24.7
412	J141157.71+520624.1	212.9905	52.1067	1.515	19.397	45.891 ± 0.000*	⋯	43.2
413	J141915.40+535522.7	214.8142	53.9230	3.340	20.791	45.601 ± 0.002	9.10 ± 0.03	28.6
414	J141402.78+540856.4	213.5116	54.1490	1.457	21.554	44.988 ± 0.003*	⋯	42.5
416	J140849.42+534050.9	212.2059	53.6808	2.600	19.870	45.621 ± 0.002	8.96 ± 0.01	39.6
418	J142148.21+525104.3	215.4509	52.8512	1.418	21.464	45.040 ± 0.003*	⋯	62.5
423	J141155.27+540435.6	212.9803	54.0766	1.521	20.626	45.296 ± 0.001*	⋯	26.3
424	J142141.25+524551.6	215.4219	52.7644	2.660	19.829	45.580 ± 0.003	8.98 ± 0.02	22.6
425	J141030.00+521307.5	212.6250	52.2188	2.574	21.273	45.306 ± 0.002	8.69 ± 0.03	22.5
426	J141032.32+535740.2	212.6347	53.9612	1.544	20.679	45.190 ± 0.002*	⋯	37.6
430	J142027.25+522431.4	215.1136	52.4087	3.919	20.416	46.150 ± 0.001	9.01 ± 0.07	41.1
431	J141551.60+520025.6	213.9650	52.0071	1.518	18.838	45.930 ± 0.001*	⋯	34.8
432	J142202.80+530034.1	215.5117	53.0095	1.391	19.890	45.429 ± 0.001*	⋯	35.7
433	J141413.27+541017.8	213.5553	54.1716	1.627	20.952	44.942 ± 0.003*	⋯	22.2
434	J140911.66+522350.1	212.2986	52.3973	1.545	20.564	45.574 ± 0.001*	⋯	53.4
435	J142102.17+533944.1	215.2591	53.6623	2.295	19.987	45.765 ± 0.001	8.58 ± 0.01	35.3
436	J142053.67+534145.2	215.2236	53.6959	1.742	20.752	45.382 ± 0.002	8.59 ± 0.01	33.0

Table 1
(Continued)

RMID	SDSS Identifier	R.A.[a] (deg) (J2000)	Decl.[a] (deg) (J2000)	z[b]	i mag[b]	log $\lambda L_{\lambda1350}$[b] (erg s^{-1})	log $M_{\mathrm{BH,SE}}$[b,c] ($M_\odot$)	S/N2[d]
441	J141531.90+515906.4	213.8829	51.9851	1.397	19.354	45.636 ± 0.001*	⋯	28.3
442	J141225.72+540741.6	213.1072	54.1282	2.152	20.355	45.244 ± 0.003	7.58 ± 0.15	24.3
445	J141114.36+520629.2	212.8098	52.1081	1.519	19.939	45.489 ± 0.001*	⋯	37.6
447	J142201.29+524824.4	215.5054	52.8068	1.707	21.088	45.199 ± 0.002	8.53 ± 0.04	22.3
448	J140725.96+525554.8	211.8582	52.9319	1.626	20.943	44.793 ± 0.003*	⋯	38.9
451	J140850.38+534611.9	212.2099	53.7700	2.674	19.340	46.031 ± 0.001	9.25 ± 0.01	30.8
452	J142214.08+531516.7	215.5587	53.2547	2.028	20.609	45.755 ± 0.001	9.08 ± 0.01	51.2
454	J142018.09+521924.9	215.0754	52.3236	2.011	18.969	45.985 ± 0.000	9.18 ± 0.01	22.4
455	J142206.84+524958.4	215.5285	52.8329	1.809	21.303	45.145 ± 0.003	8.51 ± 0.02	31.4
456	J141259.13+515925.0	213.2464	51.9903	2.266	19.958	45.677 ± 0.001	9.19 ± 0.01	29.4
461	J140830.45+534309.2	212.1269	53.7192	2.272	20.699	45.769 ± 0.001	9.14 ± 0.04	34.6
462	J140916.45+535149.3	212.3186	53.8637	1.633	21.448	44.822 ± 0.003*	⋯	23.6
467	J142140.19+523614.9	215.4175	52.6042	1.887	20.898	45.155 ± 0.003	8.47 ± 0.02	20.5
468	J140713.60+530200.8	211.8067	53.0336	3.127	20.453	45.959 ± 0.001	9.23 ± 0.02	34.5
470	J142047.48+534759.9	215.1979	53.8000	1.879	21.392	44.821 ± 0.006	8.26 ± 0.02	21.5
482	J141011.80+521002.1	212.5492	52.1673	1.530	19.580	45.733 ± 0.001*	⋯	20.7
485	J141912.47+520818.0	214.8020	52.1383	2.562	19.677	46.119 ± 0.001	9.33 ± 0.01	32.0
486	J140940.81+521337.2	212.4201	52.2270	1.401	19.702	45.626 ± 0.001*	⋯	33.6
487	J142206.54+524317.7	215.5273	52.7216	1.845	20.549	45.278 ± 0.004	8.34 ± 0.05	63.8
488	J142138.60+523324.6	215.4108	52.5568	2.604	20.250	45.712 ± 0.002	8.66 ± 0.04	42.5
490	J141058.03+540535.9	212.7418	54.0933	1.953	20.320	45.583 ± 0.001	8.96 ± 0.01	34.3
491	J140920.50+535445.5	212.3354	53.9127	1.961	20.927	45.421 ± 0.003	8.76 ± 0.03	49.4
493	J142039.47+521928.4	215.1645	52.3246	1.592	18.605	46.028 ± 0.000*	⋯	39.0
494	J142142.57+533752.3	215.4274	53.6312	1.867	21.201	45.316 ± 0.001	7.86 ± 0.20	34.7
495	J140806.04+534046.5	212.0252	53.6796	2.263	21.253	45.499 ± 0.002	9.21 ± 0.01	31.3
496	J141101.51+520402.1	212.7563	52.0673	2.080	20.508	45.560 ± 0.001	8.39 ± 0.02	21.2
499	J141004.22+540109.0	212.5176	54.0192	2.325	21.238	45.058 ± 0.003	8.37 ± 0.04	32.7
500	J141033.34+540411.4	212.6389	54.0699	1.966	21.283	45.276 ± 0.003	8.44 ± 0.02	31.1
506	J141336.30+541501.2	213.4013	54.2503	1.736	20.609	45.075 ± 0.003	8.79 ± 0.09	59.2
507	J140959.26+520912.0	212.4969	52.1533	2.575	19.780	46.212 ± 0.001	9.02 ± 0.02	26.2
508	J142129.40+522752.0	215.3725	52.4644	3.228	18.124	46.919 ± 1.000	⋯	32.9
511	J140755.91+523040.3	211.9830	52.5112	1.982	20.624	45.136 ± 0.003	8.62 ± 0.06	29.2
512	J141254.37+541410.8	213.2266	54.2363	4.328	19.394	46.518 ± 0.001	9.40 ± 0.02	41.5
514	J140945.30+521033.7	212.4388	52.1760	1.515	19.014	45.612 ± 0.001*	⋯	54.2
517	J142049.31+535211.5	215.2055	53.8699	2.216	20.200	45.839 ± 0.001	9.11 ± 0.01	39.1
520	J141924.26+540348.6	214.8511	54.0635	3.268	19.532	46.344 ± 0.000	9.45 ± 0.01	28.0
522	J142041.78+521701.6	215.1741	52.2838	1.384	20.214	45.242 ± 0.002*	⋯	32.3
527	J142226.76+524246.6	215.6115	52.7130	1.647	20.930	44.788 ± 0.003*	⋯	39.0
528	J140647.49+525956.1	211.6979	52.9989	1.820	19.777	45.170 ± 0.004	7.39 ± 0.22	21.6
529	J141317.34+541614.6	213.3223	54.2707	2.780	21.412	45.342 ± 0.003	8.78 ± 0.01	41.9
530	J142036.56+521455.0	215.1523	52.2486	2.214	21.298	45.332 ± 0.002	8.74 ± 0.02	23.0
531	J142129.53+534633.4	215.3731	53.7759	1.584	21.590	44.606 ± 0.004*	⋯	33.2
532	J140757.37+522722.2	211.9891	52.4562	2.407	20.763	45.506 ± 0.002	8.04 ± 1.09	30.8
533	J140749.14+522924.2	211.9548	52.4901	1.770	20.102	45.337 ± 0.002	8.81 ± 0.01	43.4
535	J142201.46+523250.2	215.5061	52.5473	2.122	19.781	45.737 ± 0.001	8.85 ± 0.01	45.4
538	J141806.36+515821.1	214.5265	51.9725	1.640	21.459	45.219 ± 0.001*	⋯	20.9
540	J140705.59+524250.7	211.7733	52.7141	2.747	20.206	46.019 ± 0.001	8.96 ± 0.01	42.1
542	J140908.91+535805.0	212.2871	53.9681	1.824	21.698	44.501 ± 0.025	7.50 ± 0.12	21.5
543	J142015.35+540014.5	215.0640	54.0040	2.059	20.555	45.677 ± 0.001	8.94 ± 0.01	21.7
549	J141631.45+541719.7	214.1311	54.2888	2.275	21.605	45.369 ± 0.002	8.67 ± 0.02	37.5
550	J142116.86+535114.5	215.3203	53.8540	1.879	21.218	45.113 ± 0.003	8.46 ± 0.04	23.6
553	J142301.67+531100.5	215.7570	53.1835	1.869	21.652	45.054 ± 0.003	8.60 ± 0.05	20.6
554	J141948.09+520610.5	214.9504	52.1029	1.706	20.250	45.573 ± 0.002	8.71 ± 0.01	32.4
555	J142242.59+524415.6	215.6775	52.7377	2.179	19.656	45.906 ± 0.001	9.15 ± 0.01	36.4
556	J142232.53+523938.0	215.6356	52.6606	1.494	19.416	45.525 ± 0.001*	⋯	34.9
557	J142155.20+522749.4	215.4800	52.4637	2.519	20.684	45.525 ± 0.003	8.76 ± 0.04	25.0
560	J141849.37+515950.4	214.7057	51.9973	1.867	20.927	45.131 ± 0.005	8.57 ± 0.01	34.9
561	J140853.68+535757.0	212.2237	53.9658	1.652	19.154	45.767 ± 0.001*	⋯	51.9
562	J141453.01+541952.4	213.7209	54.3312	2.786	19.392	46.302 ± 0.001	9.41 ± 0.01	39.1
563	J142113.92+521747.0	215.3080	52.2964	1.971	19.904	45.763 ± 0.001	8.96 ± 0.01	25.2
564	J142306.05+531529.0	215.7752	53.2581	2.471	18.241	46.484 ± 0.000	9.42 ± 0.01	78.4
573	J142242.14+533251.9	215.6756	53.5478	1.993	19.823	45.765 ± 0.001	8.40 ± 0.06	29.1

Table 1
(Continued)

RMID	SDSS Identifier	R.A.[a] (deg) (J2000)	Decl.[a] (deg) (J2000)	z[b]	i mag[b]	$\log \lambda L_{\lambda 1350}$[b] (erg s^{-1})	$\log M_{\mathrm{BH,SE}}$[b,c] ($M_{\odot}$)	S/N2[d]
574	J142047.87+521158.7	215.1995	52.1997	1.982	21.264	44.905 ± 0.009	7.95 ± 0.02	31.1
575	J140939.50+540532.3	212.4146	54.0923	1.625	20.530	45.417 ± 0.001*	⋯	23.8
578	J142254.99+524424.9	215.7291	52.7403	1.570	19.658	45.272 ± 0.002*	⋯	22.9
579	J140622.08+530102.0	211.5920	53.0172	2.329	21.461	45.131 ± 0.004	8.43 ± 0.03	27.7
583	J140731.08+534447.2	211.8795	53.7464	1.709	20.814	45.416 ± 0.003	8.77 ± 0.02	44.0
584	J140802.98+535154.2	212.0124	53.8651	4.058	19.120	46.646 ± 0.000	9.59 ± 0.01	44.4
585	J141609.14+514926.2	214.0381	51.8240	1.829	19.850	45.328 ± 0.002	8.74 ± 0.04	38.0
586	J140624.61+531739.7	211.6026	53.2944	2.392	21.275	45.526 ± 0.002	8.83 ± 0.02	40.7
591	J140954.00+540827.6	212.4750	54.1410	2.100	19.073	46.326 ± 0.000	9.58 ± 0.01	41.6
594	J141903.81+515800.7	214.7659	51.9669	2.934	20.414	45.731 ± 0.002	8.66 ± 0.03	22.3
595	J140613.50+530742.5	211.5563	53.1285	1.707	21.665	45.058 ± 0.005	7.22 ± 0.05	21.7
596	J140727.88+522530.9	211.8662	52.4253	1.365	19.025	45.844 ± 0.001*	⋯	27.9
600	J140617.85+531930.4	211.5744	53.3251	1.425	20.466	45.149 ± 0.003*	⋯	33.3
602	J140630.77+532753.2	211.6282	53.4648	3.115	21.354	45.428 ± 0.004	8.93 ± 0.06	38.4
609	J141952.89+520116.8	214.9704	52.0214	2.229	19.431	46.120 ± 0.001	9.13 ± 0.01	26.0
611	J142301.08+533311.8	215.7545	53.5533	1.886	17.691	46.492 ± 0.000	9.60 ± 0.01	60.7
612	J142252.42+533648.8	215.7184	53.6136	2.083	21.289	45.216 ± 0.002	8.55 ± 0.03	25.5
613	J141007.73+541203.4	212.5322	54.2010	2.336	18.120	46.591 ± 0.001	9.10 ± 0.01	55.3
614	J140904.48+520549.0	212.2687	52.0970	2.061	20.912	44.490 ± 0.016	8.24 ± 0.03	29.6
616	J141056.25+541608.5	212.7344	54.2691	2.320	19.025	46.377 ± 0.000	9.46 ± 0.01	53.5
620	J140707.30+522636.4	211.7804	52.4435	2.582	20.245	45.514 ± 0.003	8.84 ± 0.01	23.1
621	J140650.01+534023.2	211.7084	53.6731	1.774	20.995	45.031 ± 0.009	8.40 ± 0.01	30.7
623	J141727.16+514856.0	214.3632	51.8156	2.959	20.282	45.877 ± 0.002	8.83 ± 0.03	26.1
629	J142340.69+530143.1	215.9196	53.0286	1.641	21.109	44.727 ± 0.004*	⋯	26.1
630	J141838.99+515253.5	214.6625	51.8815	1.889	19.326	45.969 ± 0.000	9.16 ± 0.01	38.0
631	J140554.87+530323.5	211.4787	53.0565	2.717	19.828	46.188 ± 0.001	9.44 ± 0.04	52.9
633	J142337.51+531828.8	215.9063	53.3080	2.439	20.579	45.311 ± 0.002	8.79 ± 0.06	23.6
635	J140726.67+522013.2	211.8611	52.3370	2.595	18.908	46.405 ± 0.001	9.43 ± 0.02	37.9
636	J141102.59+541817.6	212.7608	54.3049	2.232	20.789	45.657 ± 0.001	8.49 ± 0.02	20.5
646	J140813.16+540045.3	212.0549	54.0126	1.409	20.716	45.147 ± 0.002*	⋯	21.9
647	J142318.46+533252.5	215.8269	53.5479	1.599	19.941	45.290 ± 0.001*	⋯	22.8
648	J140903.51+520307.1	212.2646	52.0520	1.788	20.590	45.170 ± 0.004	8.06 ± 0.10	23.7
651	J142149.30+521427.8	215.4554	52.2411	1.486	20.194	45.412 ± 0.001*	⋯	35.0
658	J140916.26+520022.1	212.3178	52.0062	1.947	21.473	44.577 ± 0.011	8.05 ± 0.02	30.0
660	J142342.66+524831.5	215.9278	52.8088	1.852	19.302	45.831 ± 0.001	8.31 ± 0.02	38.6
661	J141959.93+541255.3	214.9997	54.2154	2.411	20.864	45.628 ± 0.002	8.82 ± 0.02	21.5
665	J141604.84+542639.8	214.0202	54.4444	1.944	20.132	45.440 ± 0.002	8.82 ± 0.02	30.9
670	J141534.44+542730.4	213.8935	54.4585	2.021	21.340	45.388 ± 0.002	8.16 ± 0.09	27.5
676	J140904.15+541023.7	212.2673	54.1733	2.515	18.530	46.527 ± 0.001	9.82 ± 0.01	45.9
678	J142103.25+520427.0	215.2636	52.0742	1.462	19.620	45.519 ± 0.001*	⋯	29.9
680	J141940.24+515437.2	214.9177	51.9103	1.831	20.553	45.402 ± 0.002	8.38 ± 0.04	27.8
682	J142338.37+533057.4	215.9099	53.5160	1.881	21.603	45.045 ± 0.004	8.17 ± 0.02	41.0
686	J140913.79+515841.6	212.3075	51.9782	2.134	21.047	45.444 ± 0.002	8.67 ± 0.01	40.5
687	J140532.25+530401.5	211.3844	53.0671	3.072	20.958	45.586 ± 0.002	8.86 ± 0.05	36.3
688	J141129.65+514701.7	212.8735	51.7838	1.679	19.617	45.597 ± 0.001	8.37 ± 0.03	28.8
689	J140542.53+532323.5	211.4272	53.3899	2.005	21.303	45.223 ± 0.003	8.31 ± 0.01	126.8
690	J140616.09+533926.0	211.5670	53.6572	1.504	19.462	45.594 ± 0.001*	⋯	35.5
692	J142308.03+522815.5	215.7835	52.4710	1.642	19.260	45.729 ± 0.001*	⋯	33.6
693	J142043.51+520038.7	215.1813	52.0108	1.988	20.017	45.643 ± 0.001	8.82 ± 0.02	28.1
695	J140706.74+521836.3	211.7781	52.3101	1.526	21.256	44.606 ± 0.006*	⋯	24.4
698	J142350.24+532929.3	215.9594	53.4915	2.137	21.090	45.458 ± 0.002	8.82 ± 0.02	26.6
699	J141039.64+542102.9	212.6652	54.3508	2.345	20.465	45.640 ± 0.003	8.35 ± 0.03	30.4
703	J142051.98+541029.2	215.2166	54.1748	2.216	20.182	45.660 ± 0.002	8.72 ± 0.01	33.2
704	J140629.07+534625.9	211.6212	53.7739	1.649	21.179	44.990 ± 0.003*	⋯	29.3
705	J140607.57+523207.9	211.5315	52.5355	1.772	20.201	45.345 ± 0.003	9.06 ± 0.01	60.3
706	J140540.19+532850.6	211.4175	53.4807	1.774	20.479	45.316 ± 0.003	8.68 ± 0.02	30.8
710	J142418.21+530406.5	216.0759	53.0685	2.868	19.396	46.432 ± 0.001	9.43 ± 0.01	44.9
711	J140617.56+522829.4	211.5732	52.4748	1.426	20.544	45.152 ± 0.002*	⋯	37.2
713	J142411.08+532041.3	216.0462	53.3448	2.370	20.114	45.865 ± 0.001	9.04 ± 0.01	48.3
715	J142017.80+541531.4	215.0742	54.2587	1.701	19.684	45.513 ± 0.002	8.88 ± 0.01	34.5
718	J141915.05+542136.0	214.8127	54.3600	3.189	20.539	46.071 ± 0.001	9.62 ± 0.01	37.9
722	J142419.18+531750.6	216.0800	53.2974	2.509	19.494	45.799 ± 0.002	9.20 ± 0.07	44.0

Table 1
(Continued)

RMID	SDSS Identifier	R.A.[a] (deg) (J2000)	Decl.[a] (deg) (J2000)	z[b]	i mag[b]	$\log \lambda L_{\lambda 1350}$[b] (erg s^{-1})	$\log M_{\mathrm{BH,SE}}$[b,c] ($M_\odot$)	S/N2[d]
723	J140844.48+515843.3	212.1854	51.9787	1.635	20.582	45.272 ± 0.002*	⋯	39.7
725	J142322.50+522656.1	215.8438	52.4489	1.770	19.900	45.704 ± 0.001	9.19 ± 0.01	22.2
729	J142404.67+532949.3	216.0195	53.4970	2.768	19.563	46.074 ± 0.001	9.10 ± 0.01	57.9
734	J141425.95+513801.6	213.6081	51.6338	2.332	20.640	45.530 ± 0.001	9.06 ± 0.02	30.5
735	J141728.92+542849.8	214.3705	54.4805	1.829	21.147	45.081 ± 0.004	8.35 ± 0.03	29.7
737	J140648.14+535449.0	211.7006	53.9136	1.585	19.838	45.619 ± 0.001*	⋯	35.3
738	J142400.40+533347.0	216.0017	53.5631	1.599	19.986	45.478 ± 0.001*	⋯	22.6
739	J142047.88+515650.8	215.1995	51.9475	2.988	21.203	45.500 ± 0.013	8.80 ± 0.06	21.8
743	J142405.10+533206.3	216.0213	53.5351	1.730	19.181	45.389 ± 0.002	8.53 ± 0.01	38.8
748	J140906.84+515358.0	212.2785	51.8995	1.848	20.854	45.181 ± 0.003	9.02 ± 0.02	21.2
749	J140855.61+515512.2	212.2317	51.9201	2.561	20.981	45.401 ± 0.003	8.44 ± 0.02	36.8
751	J140711.71+521033.4	211.7988	52.1760	1.368	20.825	45.249 ± 0.002*	⋯	21.3
752	J142322.69+534913.5	215.8446	53.8204	1.864	20.867	45.321 ± 0.002	8.42 ± 0.02	25.6
753	J142435.26+531448.8	216.1470	53.2469	1.562	19.538	45.558 ± 0.001*	⋯	35.0
754	J142014.47+515124.3	215.0603	51.8568	1.891	20.434	45.334 ± 0.002	8.70 ± 0.01	24.0
759	J142434.46+525310.8	216.1436	52.8863	1.966	20.886	45.080 ± 0.004	8.88 ± 0.03	23.9
763	J140636.91+521614.0	211.6538	52.2706	1.634	20.282	45.196 ± 0.002*	⋯	36.8
770	J142106.86+533745.2	215.2786	53.6292	1.862	16.456	46.948 ± 0.003	9.31 ± 0.10	59.7
771	J141604.54+541039.5	214.0189	54.1777	1.492	18.642	45.841 ± 0.000*	⋯	29.2
774	J141031.12+520316.6	212.6297	52.0546	1.686	19.343	45.884 ± 0.001	8.90 ± 0.00	58.4
777	J141021.11+541452.5	212.5880	54.2479	1.402	17.680	46.170 ± 0.000*	⋯	52.8
784	J140903.64+541746.9	212.2652	54.2964	1.677	17.358	46.340 ± 0.001	9.30 ± 0.01	78.8
794	J141122.38+524154.4	212.8433	52.6984	2.386	20.899	45.350 ± 0.002	8.20 ± 0.01	25.8
796	J141807.61+534204.4	214.5317	53.7012	3.008	20.538	45.837 ± 0.001	8.92 ± 0.07	41.6
801	J140926.98+523933.3	212.3624	52.6593	1.772	20.970	44.680 ± 0.011	9.00 ± 0.06	30.8
803	J140854.31+524549.8	212.2263	52.7639	3.623	21.106	45.469 ± 0.005	8.23 ± 0.03	27.9
809	J141350.98+541028.9	213.4625	54.1747	1.659	20.750	45.204 ± 0.005	8.91 ± 0.23	32.8
810	J140735.62+524925.0	211.8984	52.8236	1.826	19.849	45.298 ± 0.004	8.22 ± 0.02	62.2
811	J141258.26+541058.8	213.2428	54.1830	1.964	19.625	46.056 ± 0.000	8.80 ± 0.01	54.3
816	J141656.69+541223.6	214.2362	54.2066	1.637	21.349	44.869 ± 0.004*	⋯	21.6
818	J141124.46+541121.3	212.8519	54.1893	1.954	19.643	45.863 ± 0.001	8.92 ± 0.01	32.5
820	J141739.09+541425.6	214.4129	54.2405	1.757	20.710	45.324 ± 0.005	8.76 ± 0.01	49.2
821	J141810.69+541301.1	214.5446	54.2170	3.511	20.720	45.978 ± 0.002	9.11 ± 0.01	37.7
827	J141218.03+541817.1	213.0751	54.3048	1.965	20.034	44.999 ± 0.006	7.99 ± 0.02	63.7
828	J141328.37+542052.8	213.3682	54.3480	2.782	20.902	45.636 ± 0.002	8.26 ± 0.06	23.0
829	J141151.56+515302.5	212.9648	51.8841	1.804	21.479	44.852 ± 0.007	8.24 ± 0.05	26.0
831	J141635.13+542141.8	214.1464	54.3616	2.130	19.419	46.043 ± 0.001	9.14 ± 0.01	21.5
835	J141302.73+542245.1	213.2614	54.3792	1.545	21.093	44.996 ± 0.002*	⋯	27.8

Notes.
[a] These measurements were made as a part of the SDSS Data Release 10 (Ahn et al. 2014).
[b] These measurements were retrieved from Shen et al. (2019b). The i magnitudes listed are PSF magnitudes, and have not been corrected for Galactic extinction. Luminosity measurements with asterisks (*) indicate measurements where L_{1350} was not available. In these cases, we converted L_{1700} to L_{1350} using measurements from Richards et al. (2006).
[c] Black hole mass uncertainties listed here include measurement uncertainties only; the estimated systematic uncertainties beyond those listed is 0.4 dex.
[d] S/N2 measurements from PrepSpec (see Section 2.1).

(This table is available in machine-readable form.)

PrepSpec also accounts for variations in seeing and small shifts in the wavelength solution. Various spectral measurements from PrepSpec using the first year of data only are presented by Shen et al. (2019b).

We use PrepSpec to improve our flux calibrations and subsequently to produce measurements of line fluxes, line widths, mean/rms profiles, and light curves for each emission line (and various continuum regions, depending on the wavelength ranges accessible for each object). We convolve our PrepSpec-corrected spectra with the SDSS filter response curves (Fukugita et al. 1996; Doi et al. 2010) to produce g- and i-band synthetic photometry for each quasar. To estimate the uncertainties in the synthetic photometric fluxes, we sum in quadrature the spectral uncertainties and the errors in the flux-correction factors reported by PrepSpec.

Before further analysis, we first removed any suspect epochs and outliers from our spectroscopic light curves. The seventh epoch is a significant outlier in a large fraction of the light curves; following Grier et al. (2017), we remove this epoch from all of our spectroscopic light curves. In addition, there are occasional spectra (roughly 4% of epochs) that have zero flux or are significant low-flux outliers in the light curves (these are cases where the BOSS spectrograph fibers were not plugged in correctly or the SDSS pipeline failed to extract a
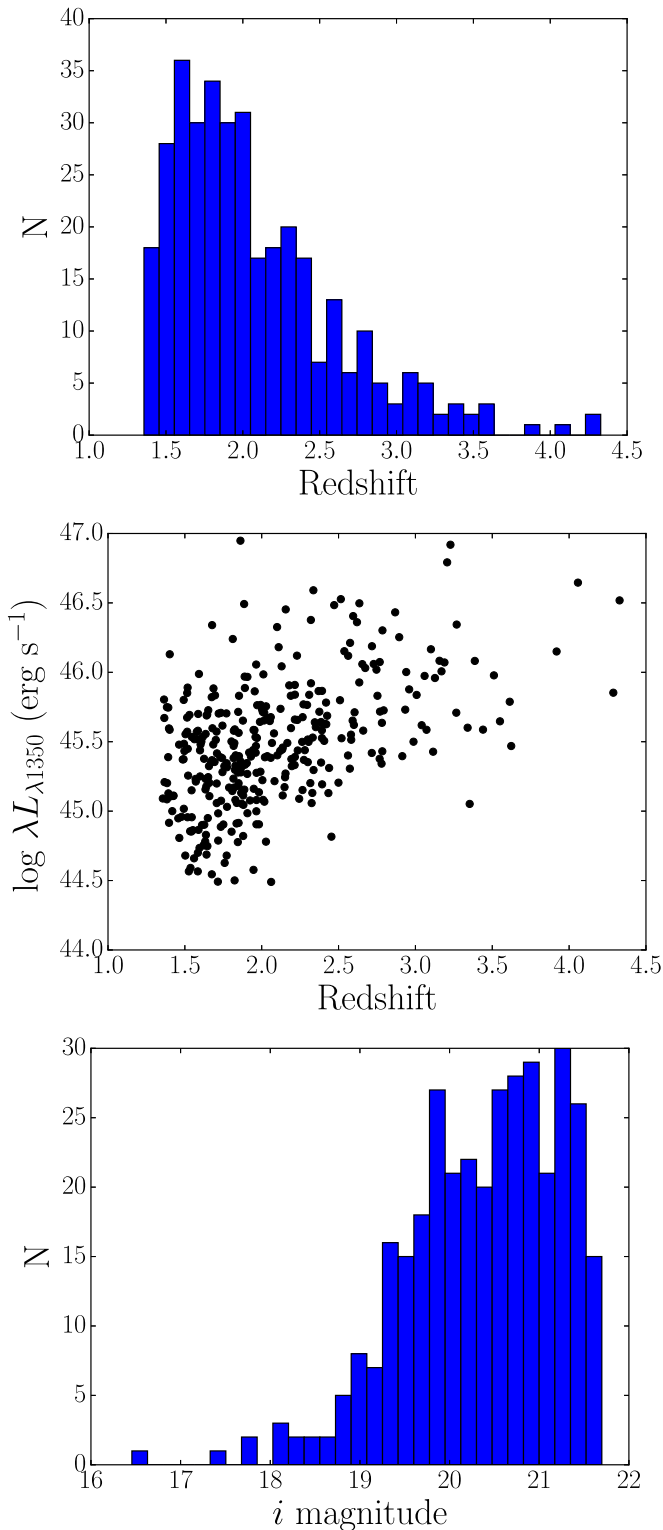
Figure 1. The distributions of various properties of our quasar sample. From top to bottom: the redshift distribution, $\lambda \log L_{\lambda 1350}$ (the continuum luminosity at 1350 Å) vs. redshift, and the distribution of i-magnitude. All quantities were measured by Shen et al. (2019b).

proper spectrum). We excluded all points with zero flux, as well as those that were offset from the median flux by more than five times the normalized median absolute deviation (NMAD) of the light curve (Maronna et al. 2006).
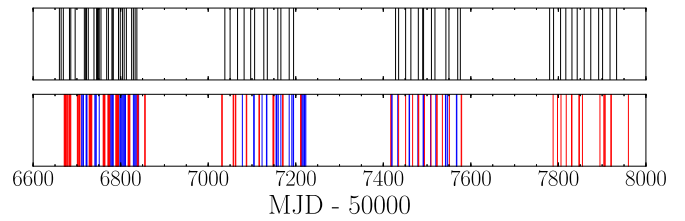
Figure 2. The distribution of MJD for the 2014–2017 spectroscopic observations from SDSS (top panel) and photometric observations from the Bok and CFHT (bottom panel). Each vertical line represents an observed epoch. Black lines indicate SDSS spectroscopic observations, blue lines represent CFHT observations, and red lines indicate Bok observations. The large spacings between sets of lines highlight the seasonal gap between each observing year.

2.3. Photometric Data

To improve the cadence of our continuum light curves, we also monitored the SDSS-RM field in the g and i bands with the Steward Observatory Bok 2.3 m telescope on Kitt Peak from 2014 to 2017, and the 3.6 m CFHT on Maunakea from 2014 to 2016. We used the Bok/90Prime instrument (Williams et al. 2004) for our observations; it has a $1° \times 1°$ field of view, mapping the observations onto a $4k \times 4k$ CCD with a plate scale of $0.''45$ pixel^{-1}. On the CFHT, we used the MegaCam instrument (Aune et al. 2003), which has a similar $1° \times 1°$ field of view and a pixel scale of $0.''187$. The observing cadence of the photometric observations is provided in Figure 2.

Following Grier et al. (2017), we adopted the image subtraction method as implemented in the software package ISIS (Alard & Lupton 1998; Alard 2000) to produce the photometric light curves. The basic steps are as follows: (1) the images are aligned; (2) the images with the best seeing, transparency, and sky background are used to create a reference image; (3) for each epoch, the reference image point-spread function (PSF) is altered to match that of the epoch, and a flux-calibration scale factor is applied to the target image; (4) the epoch and the reference image are subtracted, yielding a "difference" image that has the same flux calibration as the reference image; (5) a residual-flux light curve is produced by placing a PSF-weighted aperture over each source to measure the flux in the subtracted image.

We performed the image subtraction separately for each individual telescope, field, filter, and CCD, to obtain g- and i-band light curves for each quasar. Before further analysis, we removed problematic epochs from the light curves, such as epochs where the source fell on or near the edge of the detector, epochs where the sources were saturated or too close to a nearby saturated star, or epochs affected by cirrus clouds. As with our spectroscopy, epochs were identified as outliers in the light curves that deviated from the median flux by >5 times the NMAD of the light curve within each individual observing season (i.e., the NMAD was calculated using only data taken within a specific observing season, and outliers excluded from that season based on that NMAD alone, rather than the entire four-year light curve). We visually inspected all of the resulting light curves to confirm that this procedure was effective.

2.4. Light-curve Intercalibration and Uncertainties

To improve the precision of our continuum light curves, we placed all of the light curves from different instruments,

telescopes, fields, and in different bands onto the same flux scale —we hereafter refer to this as light-curve "intercalibration." This approach accounts for differences in detector properties, telescope throughputs, and properties specific to the individual telescopes. We combine both *g*- and *i*-band light curves together to increase the number of data points, assuming that the time lag between these two bands is negligible. Interband continuum lags have been measured for some of the SDSS-RM sample by Homayouni et al. (2019), but the measured lags are generally on the order of a week or less, which is smaller than the uncertainties for our lag measurements.

To combine our light curves, we use the Continuum REprocessing AGN MCMC (CREAM) software recently developed by Starkey et al. (2016). A brief overview of this technique is provided here; see Starkey et al. (2016) for details. CREAM models the light curves using Markov chain Monte Carlo (MCMC). The model assumes that the observed continuum emission is first emitted from a central "lamp post" and later reprocessed by more distant gas. Each telescope/ field/CCD light curve is fit to a model that includes an additive offset, scaling parameter, and transfer function (for intercali-bration purposes, we set the parameters within CREAM such that it has a delta function response at zero lag). After optimization via the MCMC fitting process, the rescaled *g* and *i* light curves are placed on the same scale as the reference light curve, and the resulting light curves are treated as a single light curve for all further analysis purposes. Figure 3 provides a demonstration of this procedure.

The final step in our light-curve preparation considers the uncertainties in our data. The ISIS image subtraction software reports only local Poisson error contributions and neglects additional systematic uncertainties; our photometric/conti-nuum light-curve uncertainties are thus generally underesti-mated by a factor of a few. Similarly, PrepSpec includes only spectral uncertainties in its emission-line flux calculations. To address this, we use an additional feature of the CREAM software that allows it to adjust the nominal error bars of the light curves. We used CREAM to search for extra variance within the light curves and apply a multiplicative correction to the uncertainties when they are underestimated. For our quasar sample, CREAM applied a median scale factor of 3.5 to correct the uncertainties in the continuum light curves and 2.6 for the emission-line light curves. We adopt the CREAM-scaled light curves and their adjusted uncertainties for all further analysis. Table 2 provides the final, intercalibrated light curves for each source with adjusted uncertainties.

2.5. Emission-line Variability Contamination

Because we are using photometric light curves (including synthetic photometry produced from spectra) to represent the continuum light curves, we also investigate the emission lines that fall within the wavelength range covered by the *g*- and *i*-band filters. The broad emission lines are expected to be variable, and strongly variable emission lines falling within the wavelength range of the filters could have a significant impact on the photometric/continuum light curve. Significant varia-bility contamination from the BLR would result in under-estimated lag measurements, effectively making it more difficult to detect a lag.

Because the lag measurements depend on the observed variability, we need to know how much of that observed variability is due to the broad emission lines instead of the
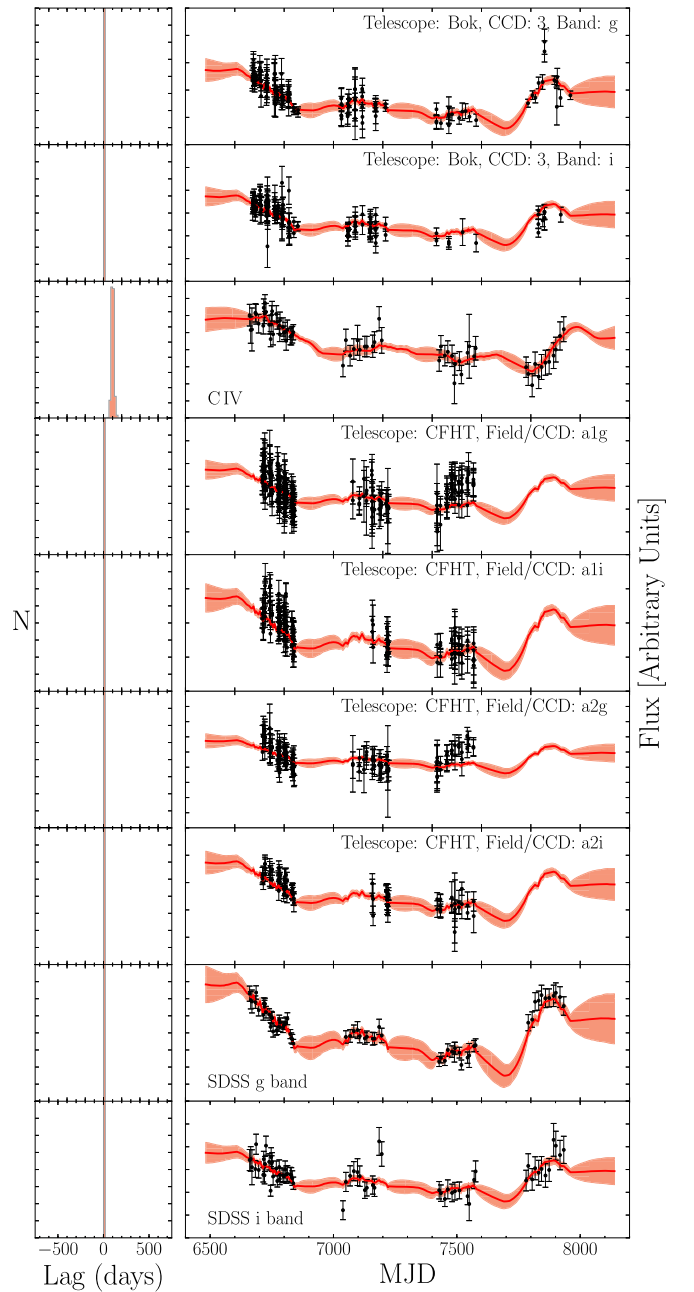

Figure 3. A demonstration of the CREAM modeling technique, using SDSS J141250.39+531719.6 (RM 052) as an example. The left panels present the CREAM posterior distributions of observed-frame time lags; the right panels show the original light curves (black filled points) with the CREAM model fits and their uncertainty envelopes (red).

continuum. To estimate this, we use the PrepSpec measure-ments of intrinsic rms variability for the broad emission lines and continuum within the wavelength range covered by the *g* and *i* filters. The "variability contamination fraction" (hereafter $f_{\rm var,BLR}$) is the sum of the variability contributions from each emission line within the FWHM of the filter: $f_{\rm var,BLR} = \sum \left(\frac{\rm rms_{line}}{\rm rms_{cont}} \right) \left(\frac{\rm EW_{line}}{\rm FWHM} \right)$. Here, $\rm rms_{line}$ and $\rm rms_{cont}$ are the PrepSpec-measured fractional rms variability of each broad emission line and the continuum nearest the filter effective wavelength, and $\rm EW_{line}$ is the observed-frame equivalent width of the emission line measured by Shen et al. (2019b). In our sources, this quantity is generally small, matching the expectation that the

Table 2
RM 000 Light Curve

MJD (−50000)	Band[a]	Telescope[b]	Flux[c]	Error[c]
6660.2090	g	S	0.99	0.06
6664.5132	g	S	1.11	0.07
6669.5005	g	S	1.21	0.08
6671.4697	g	B	0.93	0.18
6671.4717	g	B	0.87	0.17
6675.4595	g	B	1.39	0.21
6675.4619	g	B	1.46	0.20
6675.5303	g	B	1.10	0.12
6675.5327	g	B	1.23	0.13
6677.4727	g	B	1.31	0.14
6677.4751	g	B	1.02	0.15
6678.4312	g	B	1.08	0.09
6678.4336	g	B	1.06	0.09
6680.4292	g	B	1.15	0.13
6680.4316	g	B	1.20	0.13
6683.4800	g	S	0.98	0.06
6685.4228	g	B	1.13	0.05
6685.4248	g	B	1.14	0.05
6685.5239	g	B	1.17	0.04
6685.5264	g	B	1.18	0.04
6686.4736	g	S	1.14	0.07
6696.7783	g	S	1.09	0.07
6701.3901	g	B	0.76	0.21
6701.3921	g	B	0.76	0.21

Notes.

[*] Light curves for all 348 quasars can be found online. A portion are shown here for guidance in formatting.

[a] CIV = C IV emission line, g = g band, and i = i band.

[b] C = CFHT, B = Bok, S = SDSS.

[c] Continuum Flux densities and uncertainties are in units of 10^{-17} erg s^{-1} cm^{-2} Å^{-1}. Integrated emission-line fluxes are in units of 10^{-17} erg s^{-1} cm^{-2}.

(This table is available in its entirety in machine-readable form.)

continuum is more variable than the emission lines (e.g., Sun et al. 2015). We find a median variability contamination fraction of 9.1% in the g band and 1.4% in the i band in our quasar sample. In other words, the BLR contamination is negligible for most of our sources, and will generally be smaller than the measured lag uncertainties.

3. Time-series Analysis

3.1. Lag Measurements

We follow Grier et al. (2017), hereafter G17, and employ three lag detection methods to analyze our sample: The JAVELIN software (Zu et al. 2011), traditional cross-correlation functions (CCF; e.g., Peterson et al. 2004), and the CREAM software (Starkey et al. 2016). Details of each of these methods are provided in each of these works as listed; we provide only a brief synopsis of each method here.

Our primary method for time-lag detection is the JAVE-LIN code (Zu et al. 2011, 2013). We model the light curves as autoregressive processes using a damped random walk (DRW) model, which has been demonstrated to be a good description of quasar behavior on the timescales relevant to our study (e.g., Kelly et al. 2009; Kozłowski et al. 2010; MacLeod et al. 2010, 2012; Kozłowski 2016). JAVELIN accounts for all of the likely behavior of the light curves during gaps in the light

curve, and applies uncertainties to the model accordingly. JAVELIN builds a model of both the continuum and emission-line light curves while simultaneously fitting a transfer function using Markov Chain Monte Carlo techniques. We assume that the emission-line light curves are smoothed, lagged versions of the continuum light curve, and adopt a top-hat transfer function that is parameterized by a scaling factor, width, and time delay. We allow JAVELIN to explore a range of observed lags from −750 to 750 days, which is about 60% of the total length of our campaign. We then determine τ_{JAV}, the best-fit time delay, from the posterior distribution of lags produced by the MCMC chain, after some modifications that are described below (Section 3.2).

Accurately modeling the light curves requires a well-constrained damping timescale (τ_{DRW}), and for the time baseline covered by our data, this quantity is not fit well by JAVELIN—for example, using simulated light curves, Kozłowski (2017) found that the light curves must span at least 10 times τ_{DRW} in order to obtain a reliable measurement. Prior RM studies using JAVELIN have fixed the value to be longer than the length of the observing campaign (e.g., Fausnaugh et al. 2016; Grier et al. 2017), which effectively negates the impact of this on the time-lag measurements. Because the time baseline of the data in this work is longer than the expected damping timescales, however, we here allow this parameter to vary in JAVELIN, but place a strong constraint on the τ_{DRW} parameter. For each source, we calculate the expected τ_{DRW} value based on Table 1 and Equation (7) of MacLeod et al. (2010), which relates the damping timescale to the luminosity of the quasar; this expected value (typically on the order of ∼400–600 days for our sample) is fed into JAVELIN as a starting point, with small allowable uncertainties, for the MCMC step. This prevents the software from fitting unphysically small damping timescales to the data. However, the lag measurements are quite insensitive to the τ_{DRW} value fit by JAVELIN; lag measurements obtained with and without setting this constraint are almost always consistent with one another. In addition, we also fixed the width of the top-hat transfer function to 20 observed-frame days; this helps keep JAVELIN from fitting unphysical values when the top-hat width cannot be constrained by our data. We tested several different top-hat widths (ranging from 10 to 40 days), and the lag results came out consistent with one another regardless of the width chosen: Fixing the top-hat width produces more clean posterior lag distributions than when it is allowed to vary, but the exact value of the chosen width has a negligible effect on our results.

Historically, CCF methods have been used most frequently to measure RM lags, so we include these measurements for completeness and ease of comparison with prior results. However, we note that these methods have been reported to perform less well on data sets with quality similar to ours (e.g., G17; Li et al. 2019); these data have more sparse time sampling and noisy light curves, compared to much of the RM data for local AGNs. This class of methods includes the interpolated cross correlation function (ICCF; e.g., Peterson et al. 1998), the discrete correlation function (DCF; Edelson & Krolik 1988) and z-transformed DCF (zDCF; Alexander 1997). We adopted the ICCF method, as it has been used most often in previous studies and has also been shown to perform better than the DCF in cases of low sampling (White & Peterson 1994). The ICCF linearly interpolates between data points on a

user-specified grid, and the CCF is constructed by calculating the Pearson coefficient r between the two light curves at each possible lag. The centroid of the CCF ($\tau_{\rm cent}$) is measured using points surrounding the maximum correlation coefficient $r_{\rm max}$ of the CCF. We used the PyCCF code[30] (Peterson et al. 1998; Sun et al. 2018) to perform our ICCF calculations with an interpolation grid spacing of two days, and again restricted our lag search to lags between -750 and 750 days. We calculate the best lag measurement and its uncertainties via the flux randomization/random subset sampling method, using Monte Carlo simulations, as discussed by Peterson et al. (2004). We perform 5000 realizations to obtain the cross correlation centroid distribution (CCCD) and adopt the median of the distribution; the uncertainties in either direction are set to the 68th percentile of the distribution.

As an additional check, we report the lags measured by CREAM, which also measures time delays while performing the intercalibration of the light curves discussed above. CREAM is similar to JAVELIN in many ways, but it assumes a random walk model (where the Fourier transform of the time series is inversely proportional to the square of the frequency) instead of a DRW model to interpolate the light curves (Starkey et al. 2016). During the intercalibration process, CREAM fits a top-hat transfer function to the emission lines and reports the posterior probability distribution of lag values, from which we measure the best-fit lag ($\tau_{\rm CREAM}$).

3.2. Alias Identification and Removal

One of the hazards of obtaining RM data with regular seasonal gaps is the potential for lag-detection algorithms to prefer lags that result in the light curves being shifted into the seasonal gaps in the data; i.e., because RM lag detection algorithms interpolate or model within these gaps, they often end up associating features in the real continuum light curves with "fake" (i.e., model or interpolated) data in the shifted emission-line light curves. Inopportune features in the light curves can cause various lag-detection methods to latch onto incorrect lags (e.g., Grier et al. 2008). In addition, these data (and single-season data) often possess multiple significant peaks in their lag posterior distributions that can easily be identified as aliases of a primary lag solution; including the entire posterior distribution in the lag calculation in these cases often results in a skewed lag measurement and/or uncertainties that are unreasonably large.

To remedy these issues, we require additional procedures beyond simply measuring the lags from the entire posterior distributions for each method. We adopt a procedure similar to that used by G17 (see their Section 3.2), but modified to take into account the effects of seasonal gaps on the data. We apply a weight on the distribution of τ measurements in the posterior probability distributions—this weight is used to search for the primary peak of the distribution and establish a range of lags within the posterior distribution that are included in the final lag and uncertainty calculations. Our weighting procedure has two components:

1. The first component takes into account the number of overlapping spectral epochs at each time delay. Applying a time lag τ to the emission-line light curve will shift the data such that fewer "real" points will overlap. If the time

lag is such that the shift results in little or no overlap between the two data sets (for example, a τ of 180 days in data sets with regular seasonal gaps of six months), detecting that lag will be very difficult. Any potential detection of such a lag in our data has a relatively high probability of being spurious, therefore we downweight such lags in the posterior distribution. We calculate the function $P(\tau) = [N(\tau)/N(0)]^2$, where $N(\tau)$ is the number of real emission-line data points that overlap in date ranges with the continuum data and $N(0)$ is the number of overlapping points at $\tau = 0$. Thus, the weight on a lag measurement is 1 at $\tau = 0$ and decreases each time a data point moves outside the data overlap regions. Because our data have regular annual gaps of six months, $P(\tau)$ rises and falls as each segment of the light curve is shifted into and out of the overlapping ranges of each year of data.

2. The second component accounts for the effect our seasonal gaps will have on our ability to detect certain lags. To characterize this phenomenon, we compute the autocorrelation function (ACF) of the continuum variations. If the ACF declines rapidly, the annual gaps will have a significant effect on our sensitivity because we are less likely to account correctly for the light-curve behavior during the gaps. In cases where the ACF declines slowly away from zero lag, it is straightforward to interpolate across the seasonal gaps, and the gaps are thus less likely to have an effect on our lag measurements.

The final weight that we apply to the posterior distributions is thus a convolution of the continuum ACF and the $P(\tau)$ function, with one small adjustment: if the ACF drops below zero within our lag range, we set its value at that lag to zero before the convolution. Figure 4 shows two examples of these functions (one with a rapidly declining ACF and one with a slowly declining ACF). We smooth the weighted posterior lag distributions (for JAVELIN and CREAM, this is the posterior lag distribution, and in the case of the cross-correlation function, this is the CCCD) by a Gaussian kernel with a width of 15 days, and identify the tallest peak within this smoothed distribution as the "primary" peak. We identify local minima in the distribution to either side of the peak and adopt these minima as the minimum and maximum lags to be included in our final lag calculation. We then return to the *unweighted* posteriors, reject all lag samples that lie outside the determined range, and use the remaining samples to calculate the final lag and its uncertainties.

The best lag is taken to be the median of the distribution, with the uncertainty in either direction calculated using samples within the 68th percentile of the distribution. Figure 5 provides a demonstration of this procedure for one of the quasars in our sample. We tested this alias removal approach with mock light curves (with known lags) that mimic the SDSS-RM data, and found that this approach is very efficient in removing alias lags (Li et al. 2019).

3.3. Lag-significance Criteria

While our alias-removal procedure above mitigates the problem of lag aliases and seasonal gaps, these methods are not foolproof. The fact remains that, in some cases, the lags are just not well-measured, despite the models reporting their best solutions. Following G17, we thus impose a number of

---

[30] The PyCCF code is available for download at https://bitbucket.org/cgrier/python_ccf_code.
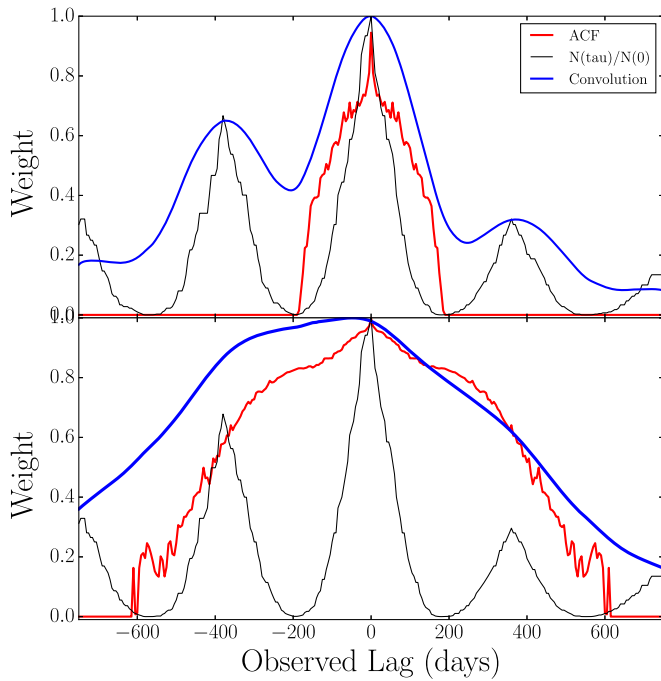
Figure 4. A demonstration of the adopted weighting scheme used in our alias removal procedure. The black line indicates $P(\tau)$, the red line shows the continuum ACF (set to zero wherever it is originally less than zero), and the thick blue line is the convolution of the two, which is our final adopted weight. The top panel shows an example where the continuum ACF declines rapidly (thus making it more unlikely that we detect spurious lags within the gaps in overlapping points); the bottom panel demonstrates a case where the continuum ACF declines slowly.

Figure 5. A demonstration of our alias removal procedure. The top two panels are the light curves for RM 119 (SDSS J141135.55+524814.4), with continuum flux density in units of in units of 10^{-17} erg s^{-1} cm^{-2} Å^{-1} and integrated emission-line fluxes in units of 10^{-17} erg s^{-1} cm^{-2}. Third panel shows the adopted weighting scheme. Bottom panel shows the original JAVELIN posterior distribution for this object (pink histogram) and the weighted posterior distribution after applying the calculated weight (blue histogram). Solid red and blue lines indicate the smoothed posterior distribution of the original and weighted posteriors, respectively. Shaded gray region highlights the range of lags included in the final lag calculation. Dashed black vertical line indicates the measured lag, and black dotted lines show the measured uncertainties.

additional criteria on our measurements for a lag to be considered a significant detection:

1. The lag can be positive or negative, but must be inconsistent with zero at 1σ significance.
2. Less than half of the posterior lag samples can be removed by our alias-removal procedure described in Section 3.2. If this procedure eliminates a larger fraction of samples, it indicates that most of the samples lie outside of the primary peak that we identified, suggesting that we lack a solid measurement of τ.
3. The behavior of the light curves must be well-correlated at or near the measured lag, as characterized by the Pearson correlation coefficient r measured by the ICCF. We include only measurements of quasars for which r reaches a value greater than 0.5 within $\pm 1\sigma$ of the reported lag (see below for a discussion of how this threshold was chosen).
4. When selecting our quasar sample, we required that the emission-line light curves showed some variability (see Section 2.1). However, after merging the light curves and adjusting the uncertainties of the light curves, some sources are no longer significantly variable. We thus require that both the continuum and emission lines are still considered significantly variable after the intercalibration process. To quantify this variability, we follow G17 and measure the rms variability S/Ns in the merged/adjusted light curves. We require that the continuum and emission-line rms variability S/N (S/N$_{con}$ and S/N$_{line}$) are greater than 6.5 and 2.0, respectively. This criterion effectively eliminates cases where the light curves are consistent with little-to-no real variability, which can result in the lag

detection methods latching onto monotonic trends or spurious correlations between noisy light curves. Roughly 20% of the 348 quasars do not meet this criterion for S/N$_{line}$. However, all but two of those sources also fail additional criteria, and would thus not have been selected as significant lags regardless.

Detailed simulations addressing the quality of lag detections yielded by our procedures are presented by Li et al. (2019). To determine the thresholds for r_{max}, S/N$_{con}$, and S/N$_{line}$, we utilize a positive/negative false-positive test as implemented by Shen et al. (2016), G17, and Li et al. (2019). We assume that there is no physical reason to measure a negative lag; if all lag measurements were due to spurious correlations rather than physical processes, we would expect to measure equal numbers of positive and negative lags in our sample (the nonuniform temporal sampling pattern in our data does not bias our results toward either positive or negative lags[31]). We can thus use the number of negative lag measurements to estimate the rate of false-positive detections at positive lags in our sample. We

---

[31] To verify this, we ran simulations using mock light curves. First, a random walk model was used to generate a continuum light curve, sampled at one-day intervals. Shifting the continuum light curve with a delay in the range -1.5 to $+1.5$ yr then provided a line light curve. These were sampled with 32 epochs in Year 1 and 12 epochs in each of Years 2–4, to approximate the SDSS-RM sampling. Synthetic data were then generated with Gaussian noise for various assumed S/N ratios. For each pair of synthetic light curves, the ICCF was computed and its peak located. The above was repeated for 1000 random-walk realizations. There is no significant difference in lag detections between positive and negative lags, indicating that our assumption above is reasonable.
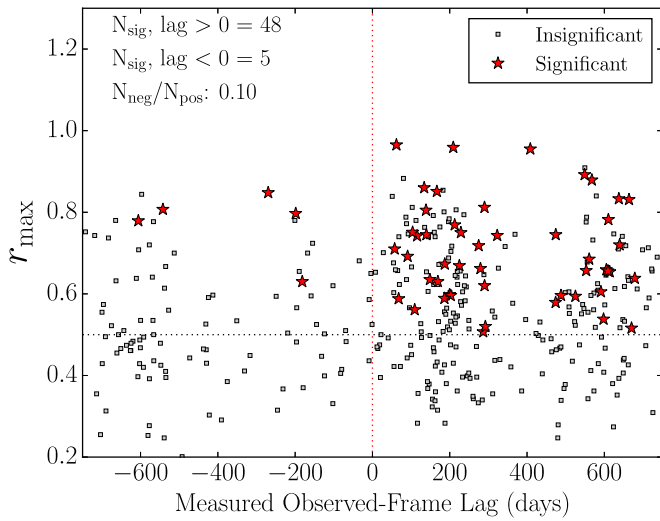
Figure 6. The measured time lag vs. r_{max} for all quasars in our sample. Those measurements that do not meet the criteria for significant lags are shown as gray points; those that meet all of the significance criteria are represented by red stars. The vertical dotted red line indicates a lag of zero, to guide the eye, and the horizontal dotted black line indicates the threshold of $r_{max} = 0.5$ used to select our significant lag sample.

define the "false-positive rate" as the ratio of negative lags to positive lags. Even including all of our lowest-quality measurements, we see a strong preference for positive lags: without imposing any selection criteria at all, we have 253 positive measurements and 95 negative measurements (see Figure 6), which indicates a false-positive rate of 37%. We provide all 348 measurements, as well as the quantities via which we measure their significance, in the Appendix in Table 5.

We choose the thresholds for our selection criteria described above in order to lower our false-positive rate to an acceptable level while maximizing the number of positive lag detections. We choose a maximum acceptable false-positive rate of 10%. Figure 6 shows the resulting distribution of lags for both those deemed "insignificant" and those passing our selection criteria. By downselecting the sample to a false-positive rate of 10%, we exclude many true lags: based on the false-positive rate without imposing our additional constraints, we expect that our sample has on the order of ∼100 additional measurable lags. Such lags may be recoverable with additional years of data.

We adopt JAVELIN as our primary lag-detection method and therefore require that all of our significance criteria are satisfied specifically for the JAVELIN measurements. This results in 48 positive lag detections and five negative measurements in our full "primary" sample of lag detections.

For comparison purposes, we apply these selection criteria separately to the lags measured with all three methods. In about 2/3 of our lag measurements, the resulting lags from all three methods are consistent with one another (see Figure 7). As reported by G17 and others (e.g., Li et al. 2019), the ICCF generally produces larger uncertainties than JAVELIN and CREAM, and the ICCF is less sensitive than JAVELIN to lag detection with light-curve qualities similar to SDSS-RM (Li et al. 2019). There has been some discussion in the literature (e.g., Edelson et al. 2019) regarding the uncertainties reported by JAVELIN; i.e., it has been suggested that JAVELIN uncertainties are underestimated. However, recent work by two independent groups suggests that the JAVELIN lag uncertainties are actually more representative of the true uncertainties than
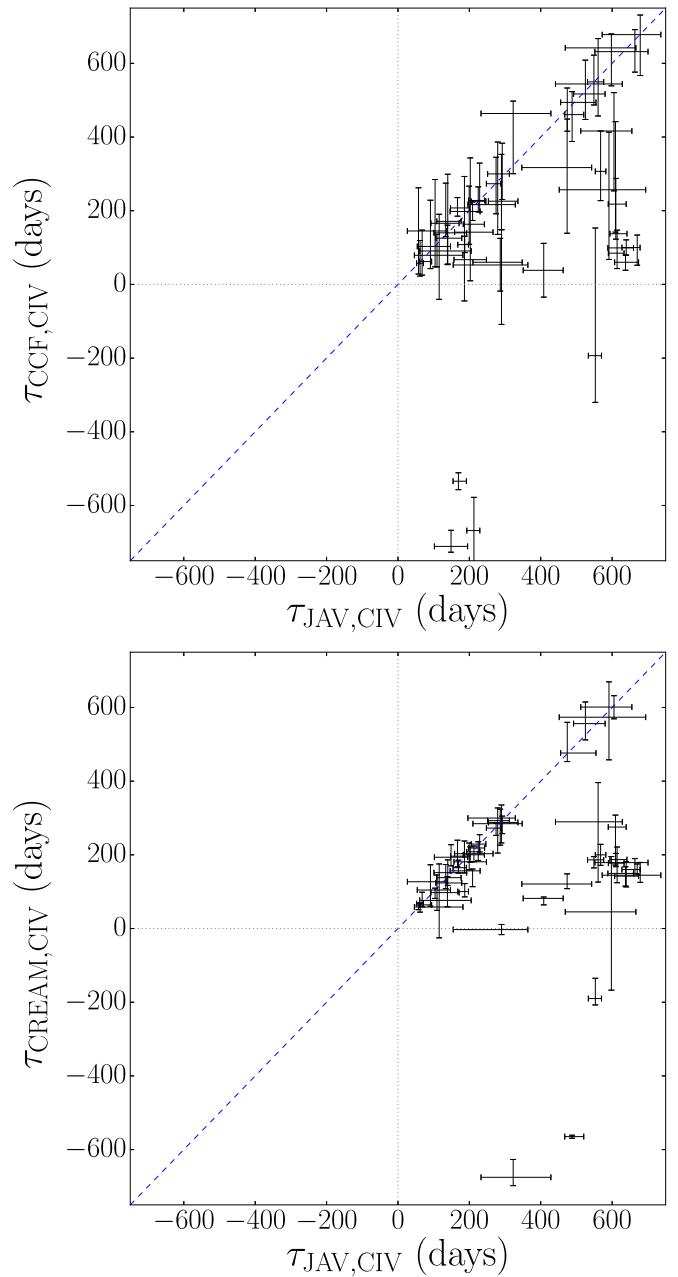

Figure 7. A comparison of the observed-frame lag measurements made using the different detection methods for our 48 positive lag detections. The top panel shows the lags measured by the ICCF vs. the JAVELIN measurements, and the bottom panel presents lags measured by CREAM vs. the JAVELIN measurements.

those reported by the ICCF method, provided that the JAVELIN assumption of Gaussian light-curve uncertainties is satisfied (Li et al. 2019; Yu et al. 2019). In addition, we note that 41 out of 48 of our significant lags were also formally detected by the ICCF method, which has been found to *overestimate* the lag uncertainties, and while we chose 1σ as our detection threshold, all but four of them are $>2\sigma$ detections. Our detections are thus robust against the possibility that the uncertainties reported by JAVELIN are underestimated to within a reasonable extent.

For about a third of our measurements, the ICCF or CREAM software reported different alias lags than JAVELIN; in these cases, a different primary peak was identified, resulting in lag disagreements. In all of these cases, we see the same

peaks present for all three methods, but their strengths vary, causing different lags to be preferred by different methods. In these cases, the different lags are frequently one-year aliases of one another. We have visually inspected all of the cases where the three measurement methods disagree, and can confirm that the peaks identified by JAVELIN are reliable in most cases. Those cases where the JAVELIN lags appear to be incorrect are taken into account with our lag measurement quality ratings (discussed in Section 3.4).

3.4. Lag Measurement Quality and the "Gold" Sample

3.4.1. Quality Ratings

Though our false-positive test (Figure 6) indicates that the majority of our lag measurements are robust, because our lag-selection procedure uses statistical arguments and we apply our criteria to achieve a false-positive rate of 10%, it is statistically likely that the lag sample presented here contains false detections. A subset of our lag detections have characteristics indicating that they are more likely to be real than others. Thus, we follow G17 and assign quality ratings to each of our measurements, in order to help readers assess the results. We use a scale of 1–5, with 1 representing the lowest-quality measurements and 5 representing the highest-quality measurements. We took into account a variety of criteria when assigning these quality ratings:

1. There are variability features visible in the continuum light curve that also appear in the emission-line light curve; i.e., it is possible to pick out a "lag" between the two light curves by eye.
2. There is clearly defined structure corresponding to the C IV emission line in the rms line profile (see Figure 12 in the Appendix).
3. The model fits from JAVELIN and CREAM match the light-curve data well, and there is general agreement in the models between the two methods.
4. The ICCF has a clear, well-defined peak on or around the measured lag.
5. There is general agreement between the three different methods used.
6. Unimodality of the posterior lag distribution: If there are several other peaks with strengths comparable to that of the peak that was determined to be the primary one, this reduces our confidence in a lag measurement.

We include these quality ratings, assigned by the first author of this work, in Table 3. In addition, we place all of the measurements with quality ratings of 4 and 5 into a "gold sample" of lag measurements that represent our highest-confidence individual measurements. Our gold sample includes 16 sources. We note that the criteria used to rate the lag measurements are subjective and based primarily on our prior experience with RM measurements. Thus, our gold sample is not statistically meaningful and should not be interpreted as such.

3.4.2. Broad Absorption-line Contamination

Because we are focused on the C IV region of the spectrum, we must also consider the possible presence of broad and narrow absorption features. PrepSpec does not currently fit absorption profiles; for narrow absorption lines, it generally has little issue interpolating across the absorption line. This will not

Table 3
SDSS-RM Observed-frame Lag Detections

RMID	z	τ_{JAV} (days)	τ_{CCF} (days)	τ_{CREAM} (days)	Quality[a] Rating
000	1.463	$322.8^{+105.6}_{-90.1}$	$463.9^{+33.7}_{-163.4}$	$-675.2^{+48.4}_{-22.6}$	2
032	1.720	$62.0^{+9.5}_{-9.8}$	$57.5^{+61.7}_{-34.8}$	$67.4^{+2.1}_{-22.8}$	5
036	2.213	$605.2^{+50.1}_{-93.1}$	$416.4^{+104.2}_{-162.5}$	$601.1^{+30.8}_{-31.9}$	1
052	2.311	$187.1^{+10.4}_{-19.4}$	$107.9^{+22.8}_{-21.7}$	$100.3^{+21.7}_{-14.4}$	4
057	1.930	$610.4^{+31.2}_{-16.5}$	$137.6^{+150.0}_{-14.8}$	$187.1^{+16.8}_{-19.2}$	1
058	2.299	$614.0^{+19.5}_{-24.4}$	$84.8^{+62.5}_{-41.8}$	$177.4^{+43.9}_{-53.0}$	1
130	1.960	$663.8^{+36.8}_{-112.1}$	$631.8^{+59.7}_{-55.6}$	$178.9^{+10.9}_{-29.4}$	2
144	2.295	$591.2^{+102.9}_{-139.3}$	$256.9^{+156.3}_{-189.2}$	$573.6^{+96.1}_{-115.7}$	2
145	2.138	$567.8^{+14.7}_{-14.9}$	$306.9^{+109.4}_{-79.5}$	$200.0^{+28.5}_{-28.4}$	3
158	1.477	$91.0^{+46.0}_{-64.6}$	$145.1^{+83.4}_{-102.1}$	$127.0^{+46.0}_{-66.3}$	3
161	2.071	$553.0^{+17.2}_{-19.5}$	$-193.4^{+346.4}_{-126.7}$	$-190.0^{+55.0}_{-17.4}$	2
181	1.678	$274.9^{+13.3}_{-27.1}$	$273.3^{+71.8}_{-81.6}$	$272.6^{+13.5}_{-19.7}$	4
201	1.797	$115.5^{+89.6}_{-54.4}$	$90.8^{+99.6}_{-131.3}$	$76.4^{+98.9}_{-101.7}$	3
231	1.646	$212.8^{+16.6}_{-20.0}$	$-668.1^{+90.1}_{-84.1}$	$208.2^{+15.8}_{-26.9}$	3
237	2.394	$169.4^{+22.4}_{-15.0}$	$-534.1^{+22.9}_{-22.9}$	$165.0^{+20.7}_{-14.5}$	2
245	1.677	$286.6^{+61.4}_{-76.6}$	$60.1^{+64.9}_{-78.3}$	$284.6^{+39.4}_{-58.2}$	2
249	1.721	$67.8^{+26.5}_{-8.3}$	$62.0^{+85.3}_{-36.8}$	$64.3^{+34.3}_{-5.5}$	4
256	2.247	$139.5^{+52.9}_{-38.7}$	$140.0^{+159.0}_{-84.7}$	$151.6^{+34.7}_{-34.7}$	5
269	2.400	$670.3^{+8.0}_{-42.8}$	$100.0^{+34.0}_{-47.9}$	$160.1^{+15.2}_{-12.5}$	1
275	1.580	$209.1^{+21.0}_{-63.0}$	$198.0^{+25.8}_{-24.5}$	$156.6^{+4.9}_{-43.0}$	5
295	2.351	$549.0^{+27.4}_{-17.9}$	$549.7^{+72.5}_{-62.7}$	$186.4^{+8.9}_{-21.9}$	3
298	1.633	$279.5^{+49.3}_{-83.5}$	$216.6^{+169.9}_{-80.9}$	$299.9^{+27.4}_{-95.1}$	4
312	1.929	$166.7^{+33.4}_{-19.5}$	$207.6^{+28.1}_{-22.4}$	$196.4^{+43.4}_{-29.1}$	4
332	2.580	$292.1^{+20.0}_{-40.9}$	$299.9^{+83.3}_{-69.5}$	$292.8^{+12.3}_{-35.3}$	4
346	1.592	$186.2^{+61.6}_{-29.3}$	$67.1^{+225.9}_{-111.9}$	$181.1^{+56.5}_{-30.2}$	3
362	1.857	$224.9^{+17.9}_{-27.2}$	$227.9^{+36.8}_{-30.8}$	$218.6^{+16.9}_{-34.1}$	2B
386	1.862	$109.4^{+37.7}_{-55.2}$	$103.1^{+32.9}_{-55.5}$	$104.5^{+40.8}_{-55.2}$	2
387	2.427	$104.0^{+67.3}_{-11.7}$	$165.9^{+118.8}_{-118.1}$	$97.5^{+12.0}_{-15.8}$	4
389	1.851	$639.5^{+20.3}_{-51.4}$	$99.1^{+21.8}_{-19.7}$	$149.6^{+31.9}_{-36.6}$	2
401	1.823	$133.8^{+43.0}_{-25.0}$	$171.1^{+103.7}_{-41.5}$	$138.1^{+35.7}_{-29.8}$	4
408	1.742	$487.9^{+32.7}_{-20.5}$	$460.8^{+62.4}_{-73.0}$	$-564.7^{+3.7}_{-4.4}$	3B
411	1.734	$678.8^{+57.7}_{-106.4}$	$677.9^{+53.2}_{-111.0}$	$144.7^{+34.7}_{-19.4}$	2
418	1.419	$199.6^{+66.9}_{-40.9}$	$141.8^{+124.9}_{-32.9}$	$203.1^{+28.9}_{-43.5}$	4
470	1.883	$57.5^{+124.6}_{-11.4}$	$79.1^{+183.2}_{-50.8}$	$58.4^{+5.2}_{-7.1}$	4
485	2.557	$474.3^{+80.5}_{-18.5}$	$494.0^{+39.0}_{-78.2}$	$476.3^{+83.3}_{-23.2}$	3
496	2.079	$609.4^{+29.9}_{-20.2}$	$217.9^{+223.9}_{-76.0}$	$275.4^{+32.4}_{-103.1}$	1
499	2.327	$560.8^{+67.8}_{-119.5}$	$544.1^{+123.1}_{-86.9}$	$289.6^{+106.4}_{-163.6}$	2
506	1.753	$637.6^{+36.5}_{-30.6}$	$60.1^{+19.7}_{-21.7}$	$142.2^{+25.3}_{-27.0}$	1
527	1.651	$138.6^{+40.1}_{-32.3}$	$125.4^{+35.3}_{-71.7}$	$123.7^{+17.2}_{-64.7}$	5
549	2.277	$228.9^{+17.4}_{-23.6}$	$225.7^{+103.6}_{-29.0}$	$229.2^{+25.5}_{-21.3}$	4
554	1.707	$525.1^{+55.2}_{-33.0}$	$517.0^{+91.7}_{-69.3}$	$556.2^{+58.7}_{-44.1}$	3
562	2.773	$597.9^{+68.7}_{-129.2}$	$642.0^{+37.9}_{-103.0}$	$45.2^{+150.2}_{-212.5}$	2
686	2.130	$202.6^{+39.4}_{-19.8}$	$163.3^{+180.0}_{-153.5}$	$200.2^{+21.6}_{-20.2}$	2
689	2.007	$474.0^{+68.7}_{-126.9}$	$317.1^{+131.7}_{-178.2}$	$120.8^{+27.5}_{-12.5}$	2
722	2.541	$148.7^{+46.4}_{-46.6}$	$-711.1^{+43.6}_{-15.8}$	$193.5^{+34.1}_{-23.4}$	1B
734	2.324	$289.9^{+46.1}_{-36.5}$	$225.9^{+127.1}_{-76.8}$	$288.0^{+47.3}_{-55.6}$	5
809	1.670	$290.1^{+73.9}_{-135.3}$	$52.7^{+95.3}_{-161.3}$	$-2.9^{+13.9}_{-16.1}$	1
827	1.966	$408.4^{+54.4}_{-57.6}$	$38.3^{+73.2}_{-72.8}$	$81.8^{+3.8}_{-17.6}$	3

Note.

[a] Lag quality rating (see Section 3.4). Quasars with significant BAL presence that affected our line width measurements (see Section 3.4.2) are identified with a "B" following their numerical rating.

affect our variability measurements, though the actual integrated emission-line flux measurements may be offset from the true values. However, BALs are a potential issue. When there

are BALs superimposed on the C IV emission line, PrepSpec is often unable to correctly interpolate over the feature and the result is that the BAL is fit as part of the continuum or emission line.

BALs are known to be variable, and they may vary simultaneously with the continuum (e.g., Barlow 1993; Lundgren et al. 2007; Filiz Ak et al. 2013; Wang et al. 2015). This may cause a light curve to be biased toward zero (or at least shorter) lags. Though studies have generally avoided BALs that are superimposed onto emission lines, due to difficulties in disentangling the two, detached BALs that are at lower velocities have been reported to be less likely to vary than those at higher velocities (e.g., Capellupo et al. 2011; Filiz Ak et al. 2013, 2014). Low-velocity troughs are also sometimes highly saturated and thus have depths that are unaffected by quasar variability. Assuming that these trends hold true for BALs at low enough velocities to overlap with the emission lines, we can expect any effect on lag measurements to be minimal in our sample (and we find that, in most cases, we measure consistent lags both with and without masking out the BAL. However, an improper fit to the C IV line profile due to the presence of a BAL will result in incorrect line width measurements, both for the mean line profile and for the rms line profile. This will in turn affect our $M_{\rm BH}$ measurements (see Section 4.3), which rely on accurate characterization of the line widths. Thus, $M_{\rm BH}$ measurements for objects whose rms profile is significantly impacted by the fit around the BAL are potentially suspect, though we note that the uncertainties in the $M_{\rm BH}$ measurements are large and the BALs may not cause deviations outside of the measurement uncertainties.

There were ten quasars in our lag-detected sample that have significant BAL components that overlap with the C IV emission line (see Figure 12). In these sources, we masked out the BAL region when fitting the spectra with PrepSpec. In three sources, we found that the C IV rms line profiles were too weak to reliably measure line widths; however, we were still able to measure a time lag in these sources. In Tables 3 and 4 and all subsequent figures, we flag these three quasars to indicate the higher uncertainty and potential for error in their measurements. In addition, the severity of the BAL contamination in all ten sources was taken into consideration when assigning the quality ratings that are reported in Table 3. These sources do not deviate systematically from the positions of the non-BAL quasars, which suggests that any effects of the BALs on our results are minimal.

4. Results and Discussion

4.1. Lag Results

We identify significant positive lags in 48 quasars in our primary sample. Of these, 16 are deemed to be high-confidence lags that constitute our "gold sample" of lag detections. All 48 positive lag measurements that constitute our sample are listed in Table 3. Light curves, model fits, and posterior lag distributions are shown for all of our positive lag detections in Figure 8.

4.2. The C IV Radius–Luminosity Relation

To place our measurements on the C IV $R_{\rm BLR}-L$ relationship, we measure $\log \lambda L_{\lambda 1350}$, the luminosity at 1350 Å, from the PrepSpec model fits. In our 10 lowest-redshift sources, 1350 Å was not covered by the spectrum; in these sources, we

measure the luminosity at 1700 Å and convert the values to $\log \lambda L_{\lambda 1350}$ by multiplying $L_{\lambda 1700}$ by factor of 1.09, which was computed from the mean quasar luminosities reported in Table 3 of Richards et al. (2006). The uncertainties on the luminosity measurements provided in Table 1 include only statistical uncertainties; due to the variability of the quasars, the actual uncertainties in the average quasar luminosities are somewhat higher. To quantify this additional source of uncertainty, we calculate the standard deviation in the flux at 1350 Å for our targets and add it to the statistical uncertainties.

Figure 9 shows the location of our sources on the $R_{\rm BLR}-L$ relation. Previous recent measurements of the relation included only ~15 sources (Lira et al. 2018; Hoormann et al. 2019); our measurements raise this number to 63. In addition, our measurements span two orders of magnitude in luminosity in a region that was previously unpopulated on the C IV $R_{\rm BLR}-L$ relation. In general, our measurements lie fairly close to the locations expected based on previously measured $R_{\rm BLR}-L$ relations.

We use the LINMIX procedure described by Kelly (2007) to fit a new relationship including our new measurements, which includes a measurement of the intrinsic scatter of the relation. We fit the relation in the form

$$\log \frac{R_{\rm BLR}}{(\text{light-days})} = a + b \times \log \frac{\lambda L_\lambda(1350\,\text{Å})}{10^{44}\,\text{erg s}^{-1}} + \epsilon, \quad (2)$$

where ϵ is the intrinsic random scatter of the relation. The resulting line fits are shown in Figure 9. Including our entire sample of significant lags, we measure a slope of $b = 0.51 \pm 0.05$, an intercept of $a = 1.15 \pm 0.08$, and an rms intrinsic scatter $\langle \epsilon^2 \rangle^{1/2} = 0.15 \pm 0.03$. Our measured slope is consistent with the most recent measurements by Lira et al. (2018) and Hoormann et al. (2019), though somewhat shallower than earlier measurements by Peterson et al. (2005) and Kaspi et al. (2007). In addition, our measured intercept is larger than that measured by Hoormann et al. (2019). Previous studies used a variety of methods to measure the line fit; for comparison purposes, we also fit our relation using the Bivariate Correlated Errors and Intrinsic Scatter (BCES) method (Akritas & Bershady 1996), implemented with the publicly available code of Nemmen et al. (2012). Results from the BCES method are consistent with those using LINMIX.[32]

Because our full sample likely includes some false-positive measurements, we also fit the relation while including only the measurements in our gold sample (see Section 3.4) and the previously reported measurements. We measure a slope of $b = 0.52 \pm 0.04$, an intercept of $a = 0.92 \pm 0.08$, and $\langle \epsilon^2 \rangle^{1/2} = 0.11 \pm 0.04$. The slope is consistent with that measured using our full sample, as well as with that measured by Hoormann et al. (2019) and Lira et al. (2018).

We caution that the fit of the $R_{\rm BLR}-L$ relation here (and in earlier work) does not take into account selection effects in the sample, which have several effects on the appearance of the $R_{\rm BLR}-L$ relation. For example, visual inspection suggests that there is some tension between our results and those at higher luminosities from Lira et al. (2018) and Hoormann et al. (2019); our measurements, when separated from the others, would

---

[32] Using the BCES method, we measure a slope of 0.49 ± 0.08 and an intercept of 1.15 ± 0.13.

Table 4
Line Width, Virial Product, and M_{BH} Measurements

RMID[a]	z	τ_{final}[b] (days)	$\sigma_{line,mean}$ (km s^{-1})	$\sigma_{line,rms}$ (km s^{-1})	FWHM$_{mean}$ (km s^{-1})	FWHM$_{rms}$ (km s^{-1})	VP ($10^7\ M_\odot$)	M_{BH}[c] ($10^7\ M_\odot$)
000	1.463	$131.1^{+42.9}_{-36.6}$	1807 ± 106	2144 ± 46	3509 ± 74	4380 ± 87	$11.8^{+5.8}_{-5.4}$	$52.6^{+25.9}_{-24.3}$
032	1.720	$22.8^{+3.5}_{-3.6}$	1805 ± 15	2017 ± 10	2768 ± 22	5010 ± 20	$1.8^{+0.7}_{-0.7}$	$8.1^{+3.2}_{-3.2}$
036	2.213	$188.4^{+15.6}_{-29.0}$	2905 ± 19	3900 ± 34	4906 ± 18	7975 ± 129	$55.9^{+21.1}_{-22.3}$	$249.9^{+94.4}_{-99.8}$
052	2.311	$56.5^{+3.1}_{-5.9}$	1397 ± 7	1322 ± 22	3258 ± 11	3354 ± 67	$1.9^{+0.7}_{-0.7}$	$8.6^{+3.2}_{-3.3}$
057	1.930	$208.3^{+10.6}_{-5.6}$	1592 ± 7	1682 ± 12	2652 ± 8	3944 ± 25	$11.5^{+4.3}_{-4.2}$	$51.4^{+19.1}_{-19.0}$
058	2.299	$186.1^{+5.9}_{-7.4}$	2695 ± 24	3412 ± 30	3564 ± 95	7512 ± 121	$42.3^{+15.6}_{-15.7}$	$189.0^{+69.9}_{-70.0}$
130	1.960	$224.3^{+12.4}_{-37.9}$	4084 ± 18	4324 ± 36	5986 ± 25	7923 ± 44	$81.8^{+30.5}_{-33.2}$	$365.8^{+136.3}_{-148.2}$
144	2.295	$179.4^{+31.2}_{-42.3}$	2830 ± 14	2792 ± 19	4419 ± 39	7222 ± 74	$27.3^{+11.1}_{-11.9}$	$122.0^{+49.7}_{-53.4}$
145	2.138	$180.9^{+4.7}_{-4.7}$	3321 ± 25	3408 ± 16	5220 ± 65	7976 ± 41	$41.0^{+15.1}_{-15.1}$	$183.3^{+67.7}_{-67.7}$
158	1.477	$36.7^{+18.6}_{-26.1}$	2043 ± 74	2136 ± 31	3621 ± 80	4888 ± 40	$3.3^{+2.0}_{-2.6}$	$14.6^{+9.1}_{-11.7}$
161	2.071	$180.1^{+5.6}_{-6.4}$	2342 ± 16	2524 ± 20	2938 ± 17	4950 ± 38	$22.4^{+8.3}_{-8.3}$	$100.1^{+37.0}_{-37.0}$
181	1.678	$102.6^{+5.0}_{-10.1}$	2116 ± 49	2721 ± 34	3024 ± 32	4533 ± 49	$14.8^{+5.5}_{-5.7}$	$66.3^{+24.6}_{-25.3}$
201	1.797	$41.3^{+32.0}_{-19.5}$	1861 ± 6	2408 ± 117	5413 ± 39	4061 ± 44	$4.7^{+4.0}_{-2.8}$	$20.9^{+17.9}_{-12.5}$
231	1.646	$80.4^{+6.3}_{-7.5}$	3326 ± 49	3803 ± 18	6496 ± 56	11792 ± 35	$22.7^{+8.5}_{-8.6}$	$101.5^{+38.2}_{-38.6}$
237	2.394	$49.9^{+6.6}_{-4.4}$	2711 ± 13	2779 ± 23	5428 ± 34	6442 ± 30	$7.5^{+2.9}_{-2.8}$	$33.6^{+13.2}_{-12.7}$
245	1.677	$107.1^{+22.9}_{-28.6}$	3910 ± 61	3953 ± 86	6847 ± 64	7031 ± 64	$32.6^{+13.9}_{-14.9}$	$145.9^{+62.2}_{-66.4}$
249	1.721	$24.9^{+9.7}_{-3.1}$	1461 ± 10	1640 ± 15	2388 ± 14	2601 ± 29	$1.3^{+0.7}_{-0.5}$	$5.8^{+3.1}_{-2.3}$
256	2.247	$43.0^{+16.3}_{-11.9}$	1720 ± 22	1802 ± 24	2440 ± 39	3565 ± 49	$2.7^{+1.4}_{-1.3}$	$12.2^{+6.4}_{-5.6}$
269	2.400	$197.2^{+2.4}_{-12.6}$	2671 ± 27	3547 ± 30	3575 ± 25	6937 ± 99	$48.4^{+17.8}_{-18.1}$	$216.4^{+79.8}_{-80.9}$
275	1.580	$81.0^{+8.2}_{-24.4}$	2027 ± 7	2406 ± 5	2992 ± 12	6943 ± 22	$9.2^{+3.5}_{-4.4}$	$40.9^{+15.6}_{-19.5}$
295	2.351	$163.8^{+8.2}_{-5.3}$	2434 ± 20	2446 ± 19	4139 ± 32	6402 ± 41	$19.1^{+7.1}_{-7.1}$	$85.5^{+31.8}_{-31.6}$
298	1.633	$106.1^{+18.7}_{-31.7}$	2045 ± 20	2549 ± 35	3176 ± 22	5177 ± 51	$13.5^{+5.5}_{-6.4}$	$60.2^{+24.6}_{-28.5}$
312	1.929	$56.9^{+11.4}_{-6.7}$	4289 ± 33	4291 ± 30	8553 ± 89	10248 ± 53	$20.5^{+8.6}_{-7.9}$	$91.4^{+38.3}_{-35.3}$
332	2.580	$81.6^{+5.6}_{-11.4}$	2945 ± 100	4277 ± 33	3813 ± 290	7828 ± 32	$29.1^{+10.9}_{-11.5}$	$130.2^{+48.8}_{-51.3}$
346	1.592	$71.9^{+23.8}_{-11.3}$	2183 ± 33	3055 ± 29	3385 ± 54	5864 ± 57	$13.1^{+6.5}_{-5.2}$	$58.5^{+29.0}_{-23.4}$
362*	1.857	$78.7^{+6.3}_{-9.5}$	3541 ± 39	4326 ± 44	5829 ± 42	12041 ± 151	$28.7^{+10.8}_{-11.1}$	$128.5^{+48.4}_{-49.8}$
386	1.862	$38.2^{+13.2}_{-19.3}$	1839 ± 26	2187 ± 41	2935 ± 31	3756 ± 70	$3.6^{+1.8}_{-2.2}$	$15.9^{+8.0}_{-10.0}$
387	2.427	$30.3^{+19.6}_{-3.4}$	2181 ± 11	2451 ± 23	3733 ± 18	4797 ± 30	$3.6^{+2.6}_{-1.4}$	$15.9^{+11.8}_{-6.1}$
389	1.851	$224.3^{+7.1}_{-18.0}$	3790 ± 12	4064 ± 15	5014 ± 49	7740 ± 27	$72.3^{+26.7}_{-27.3}$	$323.2^{+119.5}_{-121.9}$
401	1.823	$47.4^{+15.2}_{-8.9}$	2517 ± 9	3321 ± 12	3754 ± 19	10120 ± 497	$10.2^{+5.0}_{-4.2}$	$45.6^{+22.3}_{-18.8}$
408*	1.742	$177.9^{+11.9}_{-7.5}$	2519 ± 22	3872 ± 29	4130 ± 159	9227 ± 536	$52.1^{+19.5}_{-19.3}$	$232.7^{+87.1}_{-86.3}$
411	1.734	$248.3^{+21.1}_{-39.0}$	2375 ± 36	2490 ± 39	3535 ± 35	6024 ± 70	$30.0^{+11.4}_{-12.0}$	$134.3^{+50.8}_{-53.8}$
418	1.419	$82.5^{+27.6}_{-16.9}$	2542 ± 23	3110 ± 23	2952 ± 22	6159 ± 44	$15.6^{+7.8}_{-6.6}$	$69.6^{+34.7}_{-29.3}$
470	1.883	$19.9^{+43.2}_{-4.0}$	2401 ± 31	2317 ± 60	3957 ± 46	5028 ± 70	$2.1^{+4.6}_{-0.9}$	$9.3^{+20.5}_{-3.9}$
485	2.557	$133.4^{+22.6}_{-5.2}$	2919 ± 26	3961 ± 41	5422 ± 37	8535 ± 82	$40.8^{+16.6}_{-15.1}$	$182.5^{+74.0}_{-67.6}$
496	2.079	$197.9^{+9.7}_{-6.6}$	2076 ± 29	2409 ± 45	2477 ± 38	5620 ± 73	$22.4^{+8.3}_{-8.3}$	$100.2^{+37.2}_{-37.1}$
499	2.327	$168.5^{+20.4}_{-35.9}$	3007 ± 32	3085 ± 26	3233 ± 33	6371 ± 49	$31.3^{+12.1}_{-13.3}$	$139.9^{+54.3}_{-59.5}$
506	1.753	$231.6^{+13.3}_{-11.1}$	3378 ± 24	3510 ± 24	4174 ± 21	9354 ± 35	$55.7^{+20.8}_{-20.7}$	$248.9^{+92.8}_{-92.5}$
527	1.651	$52.3^{+15.1}_{-12.2}$	3380 ± 55	3587 ± 34	5263 ± 106	8306 ± 53	$13.1^{+6.1}_{-5.7}$	$58.7^{+27.5}_{-25.6}$
549	2.277	$69.8^{+5.3}_{-7.2}$	1840 ± 64	2176 ± 21	4081 ± 54	4995 ± 53	$6.5^{+2.4}_{-2.5}$	$28.8^{+10.9}_{-11.0}$
554	1.707	$194.0^{+20.4}_{-12.2}$	2286 ± 29	2229 ± 35	3636 ± 37	5609 ± 52	$18.8^{+7.2}_{-7.0}$	$84.1^{+32.2}_{-31.4}$
562	2.773	$158.5^{+18.2}_{-34.2}$	2034 ± 21	2078 ± 27	4544 ± 47	5189 ± 37	$13.4^{+5.2}_{-5.7}$	$59.7^{+23.0}_{-25.5}$
686	2.130	$64.7^{+12.6}_{-6.3}$	2126 ± 20	2203 ± 27	3839 ± 26	4847 ± 37	$6.1^{+2.6}_{-2.3}$	$27.4^{+11.4}_{-10.4}$
689	2.007	$157.6^{+22.9}_{-42.2}$	1281 ± 7	1407 ± 5	2253 ± 17	2791 ± 17	$6.1^{+2.4}_{-2.8}$	$27.2^{+10.8}_{-12.4}$
722*	2.541	$42.0^{+13.1}_{-13.2}$	3560 ± 108	8571 ± 122	6892 ± 62	17233 ± 4743	$60.2^{+29.1}_{-29.1}$	$269.1^{+130.0}_{-130.1}$
734	2.324	$87.2^{+13.9}_{-11.0}$	2978 ± 50	3405 ± 40	6296 ± 103	7042 ± 65	$19.7^{+7.9}_{-7.7}$	$88.2^{+35.4}_{-34.4}$
809	1.670	$108.6^{+27.7}_{-50.7}$	4748 ± 42	4749 ± 96	11172 ± 92	11743 ± 700	$47.8^{+21.4}_{-28.4}$	$213.7^{+95.7}_{-127.0}$
827	1.966	$137.7^{+18.3}_{-19.4}$	995 ± 9	1443 ± 13	2772 ± 19	2393 ± 134	$5.6^{+2.2}_{-2.2}$	$25.0^{+9.8}_{-9.9}$

Notes.

[a] Quasars with significant BAL inference on the C IV emission line (see Section 3.4.2) are flagged with an asterisk. These sources may have incorrect line width measurements.

[b] Measurements are in the quasar rest frame.

[c] Virial products were converted to M_{BH} using $f = 4.47$, as measured by Woo et al. (2015).

indicate a steeper slope of the relation. This tension is due to a selection effect: none of these studies is capable of measuring rest-frame lags in the 800–1000 days range within their quasar sample. Thus, the highest-luminosity end of this relation cannot currently include measurements above the measured relation and must be composed only of measurements that scatter below the
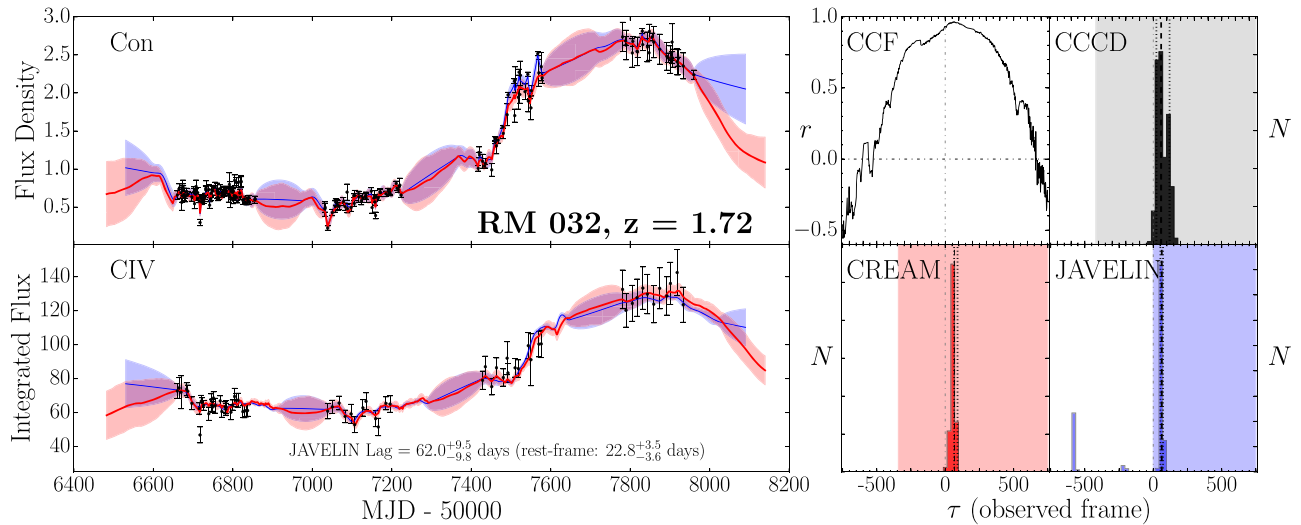
Figure 8. Light curves and posterior distributions for the quasars with significant C IV lags in our primary lag sample. The two left panels show the continuum (top) and C IV (bottom) light curves: black points are the data, blue lines show the JAVELIN model fit to the data (with the uncertainties shown as a blue envelope), and red lines show the CREAM model fit (with uncertainties shown as a red/pink envelope). For visualization purposes, data points within a single night were combined using a weighted average. Continuum flux density is provided in units of 10^{-17} erg s^{-1} cm^{-2} Å^{-1}, and integrated emission-line fluxes in units of 10^{-17} erg s^{-1} cm^{-2}. The right panels indicate the time series analysis results: the top panels show the CCF (left) and CCCD (right), and the bottom panels show the CREAM and JAVELIN posterior distributions (left and right, respectively). The measured lag and its uncertainties are indicated as dashed and dotted lines, and the shaded regions indicate the range of lags considered in the final measurement, as per our alias rejection procedure. Figures for all of our significant lag detections are provided in the figure set. Sources that are affected by BALs (see Section 3.4.2) are flagged with red "BAL" text in the bottom-left panel.

(The complete figure set (48 images) is available.)
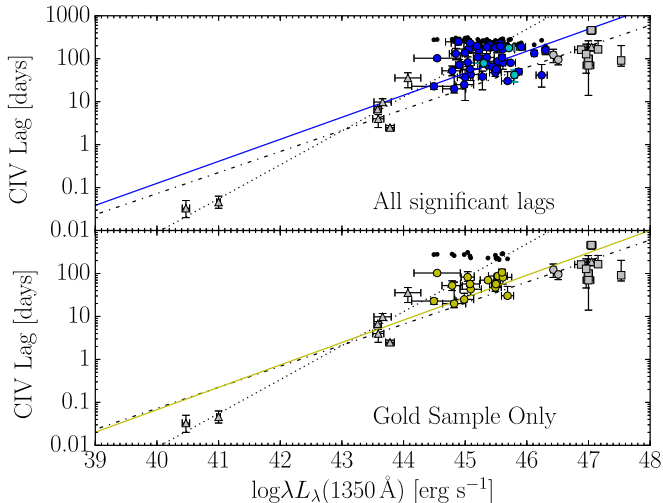
Figure 9. The CIV $R_{\rm BLR}-L$ relation. Gray solid triangles represent measurements from Peterson et al. (2004), who reanalyzed C IV data from Reichert et al. (1994), Rodriguez-Pascual et al. (1997), Korista et al. (1995), O'Brien et al. (1998), and Wanders et al. (1997), and additional measurements from Peterson et al. (2005), and Kaspi et al. (2007). Gray squares represent data from Lira et al. (2018), and gray circles indicate the two measurements from Hoormann et al. (2019). The dashed black lines show the best-fit line from Peterson et al. (2005), while the dashed–dotted black lines indicate the most recent best-fit line from Hoormann et al. (2019). In the top panel, the blue filled circles represent all of our significant lag measurements and the blue solid line indicates the measured $R_{\rm BLR}-L$ relation from the entire sample. In the bottom panel, the yellow filled circles represent only our measurements that we placed in the gold sample, and the yellow solid line represents the measured $R_{\rm BLR}-L$ relation while including only gold-sample measurements. Cyan filled circles indicate sources that are affected by BALs (see Section 3.4.2). Black solid dots represent a 750 days observed-frame lag cutoff at the redshift of each of our sources; i.e., each of our measurements has a corresponding black dot that shows the longest lag we could have detected with our campaign at that quasar's redshift (see text in Section 4.2).

relation. To fully address this issue, we require additional data for such high-luminosity sources from campaigns with extended time baselines.

Similarly, our study is unable to detect lags longer than ~750 observed-frame days. At the luminosities of most of our sources, this is long enough for us to detect lags. However, at the high-luminosity end of our sample ($\log\lambda_{L\lambda} > 45.5$), the expected rest-frame time lags based on the $R_{\rm BLR}-L$ relation are on par with the rest-frame time lag threshold for the range of redshifts of our sample. It is thus likely that we are missing some of the lags at the high-luminosity end of our sample range, due to their likely scatter above the relation (and thus above our detection threshold; this causes the apparent "flattening" effect that is visible when considering only our measurements). However, the finite observation baseline is unlikely to be affecting the detected lag measurements themselves; Figure 9 shows that the majority of our measurements fall well below the rest-frame equivalent of our 750 days detection threshold (for example, 750 observed-frame days translates to 250 rest-frame days for a quasar at a redshift of 2). This suggests that our lag measurements themselves are unlikely to be biased low due to the observed-frame lag detection limit of 750 days; if this were the case, we would expect many of our measurements to lie close to the upper detection limit. While a more detailed treatment/investigation of these issues is beyond the scope of this work, Li et al. (2019) and Fonseca Alvarez et al. (2019) have investigated this issue for the Hβ-detected lag sample using simulations, and both studies come to similar conclusions regarding selection effects for Hβ lag measurements.

Future high-luminosity measurements from data spanning long timescales will continue to shed light on the slope and scatter of the relation; however, the lack of measurements at the low-luminosity end is also problematic. The only two measurements in

sources with luminosities below 10^{43} erg s^{-1} lie below our measured relation. It could be that these measurements are consistent with the relation to within the expected intrinsic scatter; additionally, there may be an intrinsic difference in the accretion and/or line-emission region between low-luminosity sources and the high-luminosity quasars that populate much of the relation. Future RM experiments in the UV focused on local, low-luminosity AGNs would be greatly beneficial in determining whether this is the case, as well as in more concretely constraining the slope of this relation.

A more detailed quantification of the selection effects on the measured $R_{\mathrm{BLR}}-L$ relation is beyond the scope of this paper, and will be investigated with future SDSS-RM work that specifically focuses on the $R_{\mathrm{BLR}}-L$ relation using simulations similar to those performed by Li et al. (2019) and Fonseca Alvarez et al. (2019). For this reason, the preliminary C IV $R_{\mathrm{BLR}}-L$ relation presented here is primarily used as a sanity check on the bulk reliability of our C IV lags, and we do not recommend its usage for other applications (e.g., SE masses).

4.3. Black Hole Mass Measurements

For each quasar, we measure M_{BH} with Equation (1) using our adopted rest-frame time lags from JAVELIN and line widths measured by PrepSpec during the fitting process. We adopt $\sigma_{\mathrm{line,rms}}$ as our line width measurement to compute the virial product, as past studies (e.g., Peterson 2011) have suggested that $\sigma_{\mathrm{line,rms}}$ is a less biased estimator for M_{BH} than the FWHM, for a number of reasons. For example, the relationship between FWHM and σ_{line} is not linear, which can cause the underestimation of low masses and the overestimation of high masses when FWHM is used. In addition, FWHM measurements can often be significantly affected by narrow line components; see, e.g., Wang et al. (2019) for a recent discussion on this topic. However, this issue is still in contention, so we include several different characterizations of line width in Table 4. We again note that some of our objects have significant BAL contamination that has affected the PrepSpec fits (see Section 3.4.2); we flag such cases in Table 4 and caution that M_{BH} measurements for these sources may be inaccurate.

When calculating the uncertainties in the virial products, we follow G17 and add a 0.16 dex uncertainty in quadrature to the statistical uncertainties (which are calculated via standard propagation) to account for systematic uncertainties that have not been taken into account, following the 0.16 dex standard deviation among the many different mass determinations of NGC 5548 (Fausnaugh et al. 2017). To convert the virial products into M_{BH}, we adopt $f = 4.47$ (Woo et al. 2015). All virial products and M_{BH} measurements are provided in Table 4. Our M_{BH} measurements range from about 10^8 to 10^{10} solar masses, and are among the most massive SMBHs to have RM mass measurements (see Figure 10).

Figure 11 compares our RM M_{BH} measurements with SE M_{BH} estimates from Shen et al. (2019b). We add systematic uncertainties of 0.4 dex to the SE measurements to the measurement uncertainties in the Shen et al. (2019b) values (e.g., Vestergaard & Peterson 2006; Shen 2013). The SE and RM measurements are largely consistent within their (large) uncertainties for many quasars; however, there is noticeable scatter around a one-to-one relation. Our C IV lags are consistent with the previously measured $R_{\mathrm{BLR}}-L$ relation from
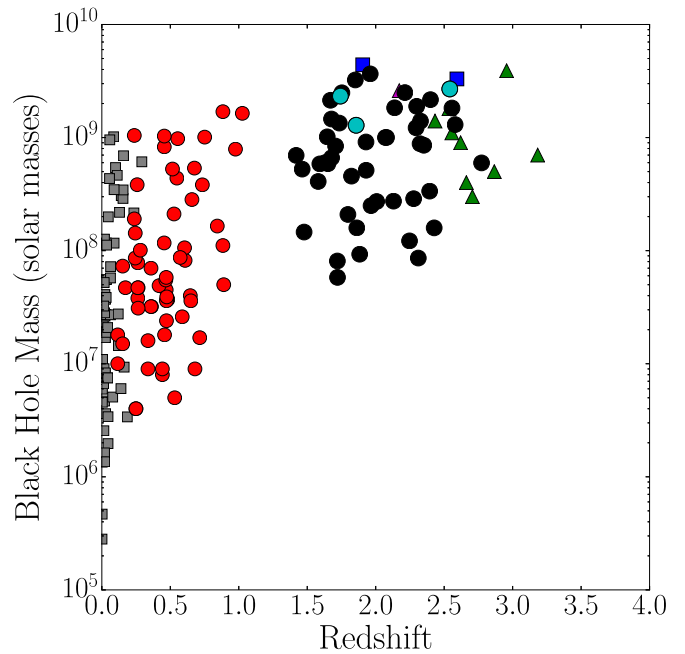

Figure 10. Black hole mass vs. redshift for reverberation-mapped AGNs. Gray squares represent Hβ RM measurements, made prior to the SDSS-RM program, by Bentz & Katz (2015) with additions from Du et al. (2016a). Red circles indicate SDSS-RM measurements made using the Hβ emission line by G17. Blue solid squares are C IV measurements by Hoormann et al. (2019), solid green triangles are C IV measurements by Lira et al. (2018), the solid magenta triangle is from Kaspi et al. (2007), and solid black circles represent C IV measurements from this work. Cyan circles indicate sources from this work that are affected by BALs (see Section 3.4.2).

which the SE estimators are derived, so we are unsurprised to see so many that are consistent; however, given the uncertainties around C IV SE M_{BH} estimates (see Section 1), we are also unsurprised to see cases with inconsistencies. A detailed analysis of the reliability of SE mass measurements is beyond the scope of this work, but will be addressed thoroughly in future work dedicated to improving SE mass estimators.

5. Summary

With four years of spectroscopic and photometric data from the SDSS-RM program, we searched for time delays between the continuum and the C IV emission-line in 348 quasars. Our main results are:

1. We measured significant positive lags in 48 quasars, with an expected false-positive detection rate of 10%. Lowering the false-positive rate threshold will yield more significant positive lags, but with increased false positives; including additional years of SDSS-RM monitoring will likely decrease the false-positive rate and lead to a larger set of lags (see Section 3.3).

2. We assigned quality ratings to each individual measurement, based on visual inspections. This led us to create a "gold sample" of 16 of our highest-confidence lag measurements (see Section 3.4). These measurements are consistent with the larger primary sample of 48 quasars, but are less likely to be false positives and so are the best sources for targeted follow-up of individual
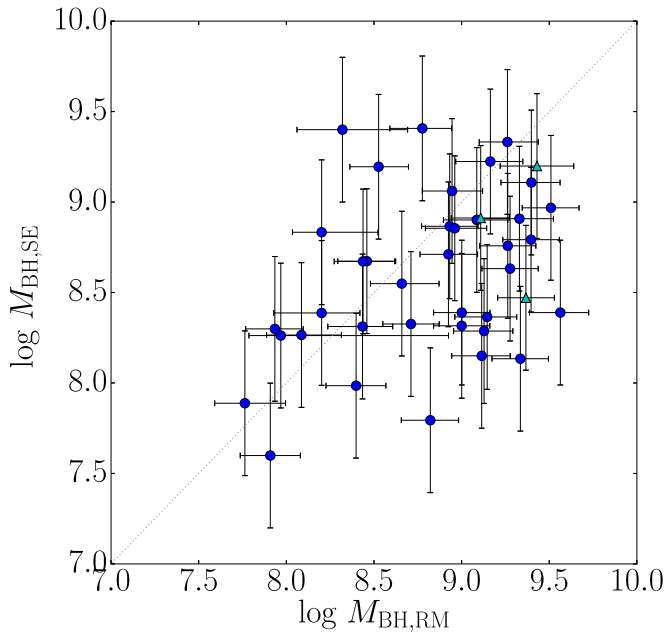
Figure 11. Single-epoch M_{BH} estimates from Shen et al. (2019b), compared to our new RM measurements. Filled blue circles represent sources without BAL contamination, and filled cyan triangles indicate sources with BALs (see Section 3.4.2). The SE values were computed using estimators from Vestergaard & Peterson (2006). We have increased the statistical uncertainties on the SE masses by 0.4 dex (see Section 4.3), to account for systematic uncertainties. The gray dotted line shows a 1:1 ratio.

quasars. We note again that the criteria used to determine this sample are subjective, and thus we caution against statistical interpretations using the gold sample.

3. We place our measurements on the C IV $R_{BLR}-L$ relation. They fill in a previously unexplored range of luminosities, and increase the number of sources included from 15–18 to ~65 (Section 4.2). We fit a new relation to our data while including the entire set of C IV RM results from the literature, and find a relation consistent with previous studies. We separately fit only the gold sample together with previous measurements, and measure a consistent relation. We caution that selection effects must be addressed before this relation can be widely used for other applications (such as designing SE mass recipes).

4. We use our time-lag measurements to obtain M_{BH} measurements for our full sample of lags (see Section 4.3). These M_{BH} values are at the high end of the distribution of RM mass measurements.

5. We have increased the sample of quasars with C IV RM lag measurements from ~18 to ~65, adding quasars at redshifts ranging from 1.35 to 2.8. This is a significant increase in both sample size and redshift range spanned by the RM sample, demonstrating the utility of multi-object RM campaigns in expanding the parameter space covered by RM observations.

We have shown here that RM measurements in quasars at higher redshifts and higher luminosities are possible, using large survey-based data sets such as ours that span multiple years. Our work makes use of four years of spectroscopic monitoring with SDSS combined with accompanying photometry from the Bok

and CFHT telescopes. The SDSS-RM program will continue to observe through 2020 as a part of the SDSS-IV program, and RM monitoring will continue through 2025 as a part of the SDSS-V Black Hole Mapper program (Kollmeier et al. 2017). The additional years of data will allow us to measure lags in quasars at higher luminosities and explore the SMBH population at unprecedented scales. In addition, we are also adding 4 yr PanSTARRS1 early light curves (2010–2014) for SDSS-RM quasars to effectively extend the baseline to measure longer lags (Shen et al. 2019a).

Beyond the SDSS-RM program and the upcoming Black Hole Mapper survey, there are several additional surveys and facilities that are planning or currently executing large RM programs using multiobject spectrographs, such as OzDES (King et al. 2015), 4MOST (Swann et al. 2019), and the Maunakea Spectroscopic Explorer (McConnachie et al. 2016). The SDSS-RM program, and our results here, serve as a proof-of-concept that such programs are not only feasible, but can have a dramatic impact on our knowledge of quasars and SMBHs across the observable universe.

Appendix

Here, we present the mean and rms spectra for our sample of significantly detected lags (Figure 12). In addition, we provide all of the measured quantities used as lag significance criteria for our entire quasar sample (Table 5).
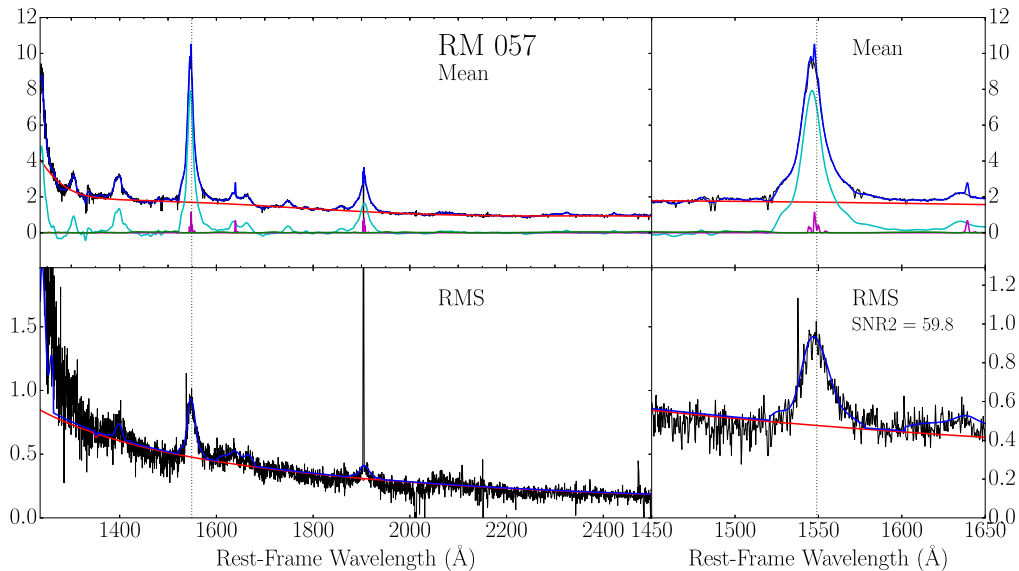
Figure 12. Mean and rms spectra for RM 057 (SDSS J141721.81+530454.3). The top panels show the mean spectrum (black), the continuum fit to the mean (red), the full model fit to the C IV emission line (blue), the BLR model (cyan), the Fe II model (green), and the narrow-line region model (magenta). The bottom panels show the rms spectra (black), the rms model (blue), and the continuum fit to the rms spectrum (red). Flux densities are in units of 10^{-17} erg s^{-1} cm^{-2} Å^{-1}. The left panels show a large portion of the observed spectrum, and the right panels show only the C IV emission-line region. Vertical dotted black lines indicate the rest-frame wavelength of the C IV emission line. Plots for all 48 of our quasars with C IV lag detections are provided in the figure set.

(The complete figure set (48 images) is available.)

Table 5
Observed-frame Lag Measurements and Significance Parameters for the Entire Sample

RMID	$\tau_{\rm JAV}$ (days)	Fraction Rejected	$r_{\rm max}$	S/N$_{\rm con}$	S/N$_{\rm line}$
000	$322.8^{+105.6}_{-90.1}$	0.23	0.54	18.00	2.72
004	$194.2^{+34.5}_{-23.5}$	0.60	0.52	8.00	0.54
006	$-124.1^{+81.1}_{-139.8}$	0.07	0.40	15.00	1.22
011	$245.4^{+89.1}_{-134.7}$	0.61	0.24	14.00	0.00
012	$13.9^{+19.3}_{-137.5}$	0.09	0.43	11.00	2.95
013	$-430.1^{+55.6}_{-39.6}$	0.70	0.46	7.00	0.56
019	$-124.1^{+117.9}_{-149.8}$	0.20	0.44	6.00	1.04
024	$524.9^{+112.3}_{-103.4}$	0.25	0.48	11.00	2.93
025	$343.3^{+47.6}_{-69.9}$	0.27	0.72	7.00	1.44
028	$157.7^{+47.8}_{-46.3}$	0.13	0.40	13.29	3.62
031	$162.2^{+105.9}_{-123.8}$	0.06	0.74	12.00	1.18
032	$62.0^{+9.5}_{-9.8}$	0.23	0.96	16.00	4.84
034	$396.5^{+132.3}_{-154.9}$	0.06	0.39	14.00	2.33
035	$102.9^{+110.4}_{-13.1}$	0.06	0.81	16.00	1.17
036	$605.2^{+50.1}_{-93.1}$	0.06	0.56	11.25	4.01
038	$-472.7^{+151.4}_{-115.3}$	0.42	0.42	11.00	0.00
039	$-577.2^{+34.7}_{-49.6}$	0.49	0.69	0.00	4.75
041	$28.2^{+52.4}_{-15.6}$	0.01	0.70	15.67	1.58
045	$-82.2^{+142.1}_{-73.4}$	0.00	0.41	0.00	1.79
049	$-412.9^{+48.8}_{-79.7}$	0.50	0.46	11.00	0.05
051	$535.6^{+8.5}_{-8.3}$	0.32	0.30	7.50	3.54
052	$187.1^{+10.4}_{-19.4}$	0.29	0.51	9.50	3.42
055	$698.9^{+41.7}_{-161.7}$	0.31	0.71	10.00	0.00
057	$610.4^{+31.2}_{-16.5}$	0.37	0.57	11.67	2.46
058	$614.0^{+19.5}_{-24.4}$	0.31	0.58	9.00	3.05
059	$219.9^{+89.0}_{-26.4}$	0.63	0.38	15.33	0.16
063	$509.5^{+72.2}_{-46.0}$	0.47	0.55	0.00	1.92
064	$627.3^{+21.6}_{-52.6}$	0.04	0.42	7.50	2.14
065	$316.6^{+30.1}_{-58.5}$	0.09	0.53	9.00	1.66
066	$-604.9^{+10.9}_{-17.0}$	0.70	-0.04	23.00	4.97
069	$155.5^{+193.8}_{-88.1}$	0.06	0.34	11.00	1.11
071	$554.1^{+83.8}_{-107.1}$	0.06	0.65	12.25	1.54
072	$22.0^{+34.3}_{-194.3}$	0.09	0.50	12.50	1.71
075	$-179.3^{+298.9}_{-142.1}$	0.09	0.37	12.50	1.55
076	$218.8^{+17.7}_{-16.8}$	0.57	0.59	14.50	4.86
079	$-330.9^{+13.0}_{-16.9}$	0.26	0.41	14.00	2.04
080	$547.1^{+50.7}_{-31.3}$	0.64	0.44	7.50	3.98
081	$-167.7^{+105.2}_{-46.0}$	0.41	0.59	12.50	0.21
086	$-577.1^{+13.4}_{-10.0}$	0.58	0.24	23.00	3.29
087	$143.1^{+137.3}_{-66.6}$	0.68	0.23	7.00	0.00
092	$172.4^{+14.9}_{-17.8}$	0.20	0.47	20.00	1.00
095	$508.4^{+31.3}_{-34.6}$	0.04	0.60	0.00	1.94
097	$182.6^{+40.1}_{-62.0}$	0.73	0.85	14.00	3.40
098	$-742.5^{+20.5}_{-6.5}$	0.00	0.75	6.00	4.86
107	$-713.7^{+19.5}_{-7.5}$	0.27	0.26	7.00	1.31
108	$199.1^{+29.3}_{-40.8}$	0.60	0.34	14.00	3.28
110	$182.9^{+47.5}_{-36.4}$	0.14	0.45	14.00	0.76
112	$101.2^{+8.9}_{-14.6}$	0.52	0.67	10.00	3.04
116	$170.8^{+60.6}_{-24.7}$	0.69	0.52	13.00	1.84
117	$-565.8^{+77.0}_{-128.1}$	0.05	0.44	18.00	0.00
119	$186.5^{+35.3}_{-42.3}$	0.19	0.56	15.50	1.35
124	$-601.9^{+4.5}_{-4.7}$	0.56	0.21	14.00	4.06
128	$565.3^{+18.7}_{-21.9}$	0.16	0.44	19.00	2.77
130	$663.8^{+36.8}_{-112.1}$	0.13	0.83	16.50	2.45
137	$269.0^{+21.3}_{-70.2}$	0.01	0.47	6.00	4.21
142	$88.2^{+113.6}_{-132.6}$	0.00	0.77	14.00	0.00

Table 5
(Continued)

RMID	$\tau_{\rm JAV}$ (days)	Fraction Rejected	$r_{\rm max}$	S/N$_{\rm con}$	S/N$_{\rm line}$
144	$591.2^{+102.9}_{-139.3}$	0.13	0.54	8.50	2.11
145	$567.8^{+14.7}_{-14.9}$	0.09	0.79	21.00	3.92
149	$-131.5^{+65.4}_{-41.1}$	0.44	0.33	9.00	1.42
150	$543.9^{+45.7}_{-31.1}$	0.35	0.57	15.00	1.65
153	$557.7^{+72.7}_{-99.6}$	0.27	0.56	10.00	0.00
154	$-566.6^{+7.7}_{-5.7}$	0.09	-0.24	12.00	4.35
155	$498.8^{+114.3}_{-69.2}$	0.04	0.38	12.00	0.51
156	$555.6^{+54.6}_{-65.4}$	0.21	0.43	11.00	0.78
157	$118.0^{+16.2}_{-12.5}$	0.46	0.31	9.50	1.55
158	$91.0^{+46.0}_{-64.6}$	0.10	0.68	12.00	2.08
159	$517.2^{+36.2}_{-15.8}$	0.31	0.43	10.00	2.99
161	$553.0^{+17.2}_{-19.5}$	0.29	0.54	7.50	2.56
164	$598.5^{+18.3}_{-36.5}$	0.25	0.41	0.00	4.89
172	$88.1^{+411.2}_{-108.5}$	0.27	0.64	12.75	0.00
176	$-689.4^{+28.5}_{-28.3}$	0.29	0.31	13.00	0.59
178	$329.7^{+277.4}_{-55.5}$	0.10	0.44	11.50	2.86
179	$-610.8^{+27.7}_{-22.2}$	0.65	0.14	12.00	0.00
180	$-437.3^{+31.6}_{-57.9}$	0.64	0.13	11.00	1.82
181	$274.9^{+13.3}_{-27.1}$	0.13	0.72	13.00	3.38
182	$228.2^{+191.3}_{-19.8}$	0.05	0.56	26.00	1.53
186	$623.6^{+67.4}_{-111.5}$	0.55	0.24	9.00	2.46
190	$-200.7^{+4.9}_{-4.9}$	0.71	0.60	9.00	5.41
194	$80.2^{+29.8}_{-7.2}$	0.80	0.87	21.00	1.19
196	$-538.8^{+24.0}_{-29.8}$	0.47	0.23	6.00	0.00
201	$115.5^{+89.6}_{-54.4}$	0.01	0.72	16.50	3.23
202	$495.7^{+28.0}_{-29.5}$	0.36	0.37	14.00	2.68
205	$484.6^{+31.0}_{-51.9}$	0.10	0.29	21.00	4.11
207	$-718.6^{+35.3}_{-18.6}$	0.60	0.74	14.50	2.37
208	$-144.6^{+42.5}_{-49.5}$	0.61	0.38	3.00	2.80
210	$154.7^{+223.1}_{-232.6}$	0.42	0.24	9.00	0.00
213	$269.9^{+182.0}_{-56.2}$	0.34	0.29	0.00	1.57
216	$573.0^{+42.3}_{-51.4}$	0.04	0.36	14.00	2.01
217	$40.8^{+142.9}_{-23.9}$	0.49	0.49	6.50	2.51
218	$233.3^{+73.1}_{-52.5}$	0.42	0.45	11.00	0.00
220	$11.8^{+129.4}_{-107.7}$	0.57	0.47	13.00	0.97
222	$624.5^{+45.6}_{-40.7}$	0.11	0.75	16.00	0.07
225	$59.5^{+35.7}_{-29.2}$	0.26	0.54	9.00	1.75
226	$-8.5^{+85.5}_{-124.5}$	0.59	0.59	1.50	1.55
227	$652.2^{+11.6}_{-9.1}$	0.54	0.53	10.50	2.81
230	$202.3^{+67.2}_{-40.2}$	0.09	0.47	16.50	1.40
231	$212.8^{+16.6}_{-20.0}$	0.47	0.54	17.00	4.71
237	$169.4^{+22.4}_{-15.0}$	0.40	0.59	20.00	2.90
238	$7.7^{+130.9}_{-127.5}$	0.14	0.65	18.50	1.46
241	$713.8^{+15.9}_{-24.2}$	0.57	0.29	16.00	4.11
242	$69.7^{+69.2}_{-67.5}$	0.47	0.49	8.00	1.34
244	$125.1^{+10.9}_{-8.4}$	0.28	0.53	0.00	4.75
245	$286.6^{+61.4}_{-76.6}$	0.01	0.51	12.00	2.30
249	$67.8^{+26.5}_{-8.3}$	0.36	0.59	8.50	3.98
251	$162.7^{+54.2}_{-16.5}$	0.74	0.35	11.00	3.09
253	$646.4^{+53.6}_{-48.2}$	0.20	0.31	13.00	2.24
256	$139.5^{+52.9}_{-38.7}$	0.14	0.71	15.00	3.42
257	$20.6^{+30.4}_{-35.9}$	0.11	0.23	8.33	1.40
259	$572.3^{+29.0}_{-24.5}$	0.12	0.39	11.00	0.43
262	$-492.4^{+15.7}_{-58.5}$	0.30	0.20	3.50	2.04
264	$549.6^{+10.7}_{-10.1}$	0.03	0.04	15.00	3.62
266	$-664.4^{+93.0}_{-6.2}$	0.66	0.26	12.00	2.26
269	$670.3^{+8.0}_{-42.8}$	0.14	0.51	8.00	4.33

Table 5
(Continued)

RMID	$\tau_{\rm JAV}$ (days)	Fraction Rejected	$r_{\rm max}$	S/N$_{\rm con}$	S/N$_{\rm line}$
275	$209.1^{+21.0}_{-63.0}$	0.42	0.95	18.33	4.73
279	$-548.6^{+26.4}_{-28.0}$	0.52	0.40	17.00	1.21
280	$55.2^{+88.9}_{-136.2}$	0.39	0.60	14.20	0.00
282	$386.1^{+25.2}_{-38.0}$	0.22	0.29	4.50	0.00
283	$193.6^{+69.5}_{-33.5}$	0.06	0.38	8.50	3.62
284	$-34.2^{+34.9}_{-28.8}$	0.47	0.68	6.00	2.06
286	$260.9^{+35.4}_{-29.0}$	0.23	0.34	0.00	4.38
293	$584.4^{+34.7}_{-30.3}$	0.18	0.43	13.00	2.79
295	$549.0^{+27.4}_{-17.9}$	0.45	0.89	18.00	2.88
298	$279.5^{+49.3}_{-83.5}$	0.08	0.66	17.00	3.18
304	$284.2^{+76.5}_{-18.6}$	0.22	0.25	10.00	0.00
310	$-703.6^{+18.8}_{-24.8}$	0.60	0.21	16.00	2.33
312	$166.7^{+33.4}_{-19.5}$	0.28	0.85	22.00	4.90
317	$126.8^{+65.2}_{-12.9}$	0.24	0.49	12.00	1.10
318	$215.8^{+70.3}_{-66.8}$	0.43	0.48	18.67	1.72
319	$197.1^{+43.8}_{-40.1}$	0.07	0.69	10.00	0.53
321	$55.8^{+63.4}_{-73.0}$	0.62	0.29	10.33	1.37
322	$200.7^{+33.7}_{-32.1}$	0.41	0.60	4.00	1.62
327	$-626.4^{+69.3}_{-79.1}$	0.56	0.46	20.67	0.82
330	$423.3^{+90.6}_{-81.9}$	0.14	0.50	16.75	0.00
332	$292.1^{+20.0}_{-40.9}$	0.09	0.52	9.50	4.54
334	$135.0^{+85.0}_{-162.2}$	0.17	0.76	11.00	1.67
335	$236.7^{+15.6}_{-30.3}$	0.53	0.78	11.00	3.89
339	$441.0^{+193.7}_{-404.1}$	0.14	0.49	10.00	0.87
342	$498.6^{+157.1}_{-166.6}$	0.02	0.60	7.00	0.82
343	$660.9^{+49.5}_{-119.8}$	0.22	0.64	13.00	0.00
344	$205.3^{+153.1}_{-91.6}$	0.00	0.72	9.00	0.00
345	$171.8^{+80.7}_{-56.3}$	0.66	0.67	4.00	2.46
346	$186.2^{+61.6}_{-29.3}$	0.00	0.58	7.00	2.41
348	$-547.5^{+35.8}_{-29.0}$	0.55	0.42	5.00	3.12
349	$-537.9^{+196.7}_{-87.7}$	0.40	0.38	0.00	0.31
351	$662.4^{+12.7}_{-19.4}$	0.14	0.36	8.00	3.72
353	$-566.1^{+14.4}_{-13.8}$	0.54	0.04	17.00	1.46
358	$216.4^{+46.9}_{-47.7}$	0.57	0.72	7.00	1.21
359	$-636.5^{+119.9}_{-100.5}$	0.62	0.41	8.67	0.35
361	$-154.8^{+144.3}_{-59.3}$	0.04	0.66	11.50	1.58
362	$224.9^{+17.9}_{-27.2}$	0.21	0.67	15.50	3.92
363	$-245.8^{+31.1}_{-39.2}$	0.08	0.26	10.50	2.44
366	$-527.3^{+28.9}_{-21.3}$	0.55	0.52	9.00	2.95
372	$185.3^{+45.2}_{-33.2}$	0.60	0.76	15.67	3.92
379	$-158.7^{+15.8}_{-33.0}$	0.35	0.59	12.00	1.01
380	$160.0^{+10.5}_{-9.3}$	0.34	0.59	15.00	1.91
381	$288.4^{+122.1}_{-64.8}$	0.01	0.65	16.00	1.07
383	$230.3^{+29.4}_{-41.3}$	0.37	0.23	0.00	1.50
386	$109.4^{+37.7}_{-55.2}$	0.49	0.56	11.00	2.21
387	$104.0^{+67.3}_{-11.7}$	0.30	0.75	12.00	2.26
389	$639.5^{+20.3}_{-51.4}$	0.10	0.52	12.67	3.08
394	$-231.4^{+76.3}_{-109.1}$	0.27	0.34	5.00	1.13
396	$-675.4^{+97.5}_{-67.5}$	0.80	0.26	2.50	0.00
397	$708.5^{+11.4}_{-11.8}$	0.24	0.13	5.00	3.17
401	$133.8^{+43.0}_{-25.0}$	0.33	0.84	12.00	3.39
403	$723.5^{+12.4}_{-55.0}$	0.66	0.65	8.00	3.56
405	$722.5^{+18.5}_{-62.9}$	0.27	0.46	16.00	1.72
408	$487.9^{+32.7}_{-20.5}$	0.07	0.60	10.00	4.47
409	$126.3^{+21.9}_{-20.2}$	0.29	0.35	10.75	2.72
410	$-542.1^{+26.4}_{-45.6}$	0.10	0.81	15.33	3.39
411	$678.8^{+57.7}_{-106.6}$	0.11	0.64	14.00	3.15
412	$368.9^{+97.5}_{-34.9}$	0.01	0.75	16.67	0.15
413	$523.1^{+17.8}_{-19.4}$	0.42	0.34	2.00	3.11
414	$219.5^{+47.2}_{-40.2}$	0.07	0.62	21.00	1.93
416	$-699.1^{+36.2}_{-31.2}$	0.72	0.43	10.50	0.93
418	$199.6^{+66.9}_{-40.9}$	0.20	0.60	12.00	2.33
423	$-625.2^{+52.0}_{-32.6}$	0.18	0.45	11.00	4.16
424	$433.4^{+73.7}_{-60.7}$	0.55	0.53	3.00	3.04
425	$142.3^{+153.3}_{-122.5}$	0.44	0.26	0.00	1.32
426	$216.2^{+330.7}_{-354.3}$	0.00	0.47	19.00	0.00
430	$158.4^{+60.1}_{-62.1}$	0.20	0.62	5.50	3.02
431	$116.5^{+385.2}_{-261.2}$	0.20	0.28	12.00	0.00
432	$-699.7^{+24.9}_{-6.4}$	0.47	0.56	15.00	1.87
433	$214.3^{+43.7}_{-52.9}$	0.45	0.46	17.00	1.58
434	$-580.7^{+22.8}_{-16.4}$	0.62	0.25	7.00	2.97
435	$-195.9^{+14.5}_{-21.1}$	0.16	0.18	15.50	3.42
436	$487.7^{+147.2}_{-162.5}$	0.13	0.35	6.50	1.08
441	$570.3^{+24.7}_{-22.9}$	0.09	0.67	11.33	0.58
442	$-599.9^{+10.3}_{-37.2}$	0.52	0.50	8.00	2.65
445	$189.8^{+15.4}_{-12.2}$	0.50	0.34	15.00	3.73
447	$-643.2^{+40.5}_{-35.5}$	0.59	0.49	8.50	0.48
448	$-535.0^{+46.7}_{-95.1}$	0.65	0.41	10.00	1.02
451	$-424.4^{+102.3}_{-95.7}$	0.67	0.49	11.33	0.00
452	$-624.6^{+72.2}_{-36.3}$	0.31	0.48	13.00	1.44
454	$99.0^{+388.6}_{-51.9}$	0.03	0.33	7.67	1.63
455	$579.1^{+24.1}_{-19.2}$	0.27	0.00	11.50	4.39
456	$174.6^{+28.4}_{-13.5}$	0.74	0.62	8.00	2.94
461	$-431.1^{+69.5}_{-116.0}$	0.47	0.40	8.00	0.52
462	$662.0^{+19.4}_{-138.9}$	0.32	0.33	7.00	2.76
467	$-657.0^{+85.3}_{-46.7}$	0.57	0.44	15.00	1.47
468	$-569.5^{+56.2}_{-47.5}$	0.25	0.64	6.50	2.09
470	$57.5^{+124.6}_{-11.4}$	0.04	0.71	17.00	2.72
482	$186.3^{+28.7}_{-20.5}$	0.48	-0.07	12.40	2.58
485	$474.3^{+80.5}_{-18.5}$	0.21	0.74	12.33	2.20
486	$242.9^{+86.6}_{-48.0}$	0.38	0.23	17.67	1.76
487	$51.2^{+103.4}_{-14.3}$	0.57	0.84	10.50	3.81
488	$209.3^{+71.8}_{-37.3}$	0.10	0.16	12.00	1.95
490	$553.0^{+25.1}_{-30.4}$	0.15	0.15	12.67	1.77
491	$725.6^{+18.1}_{-51.9}$	0.66	0.31	0.00	0.77
493	$-661.2^{+46.5}_{-34.1}$	0.45	0.46	8.80	0.00
494	$-577.3^{+2.9}_{-3.3}$	0.52	-0.55	4.00	0.00
495	$-429.3^{+302.9}_{-203.4}$	0.34	0.43	11.00	0.19
496	$609.4^{+29.9}_{-20.2}$	0.20	0.53	11.50	4.86
499	$560.8^{+67.8}_{-119.5}$	0.07	0.69	7.00	2.12
500	$167.3^{+80.5}_{-35.0}$	0.19	0.38	14.00	0.00
506	$637.6^{+36.5}_{-30.6}$	0.22	0.57	11.50	3.59
507	$576.6^{+98.6}_{-188.4}$	0.13	0.52	9.50	0.00
508	$-651.1^{+11.0}_{-9.7}$	0.74	0.28	9.11	2.27
511	$249.2^{+132.1}_{-99.0}$	0.74	0.41	5.00	1.59
512	$-535.1^{+121.5}_{-100.0}$	0.14	0.08	0.00	1.52
514	$462.2^{+176.9}_{-293.1}$	0.23	0.49	9.00	0.00
517	$227.1^{+81.6}_{-125.3}$	0.09	0.66	11.33	1.52
520	$604.2^{+92.9}_{-101.3}$	0.29	0.65	9.00	0.00
522	$237.8^{+63.0}_{-77.4}$	0.36	0.52	8.00	0.36
527	$138.6^{+40.1}_{-32.3}$	0.00	0.81	10.00	4.22
528	$-592.6^{+97.9}_{-87.2}$	0.66	0.35	6.00	0.00
529	$439.5^{+17.1}_{-13.0}$	0.53	0.32	7.00	3.32
530	$101.3^{+9.8}_{-36.8}$	0.79	0.45	7.00	2.59

Table 5
(Continued)

RMID	$\tau_{\rm JAV}$ (days)	Fraction Rejected	$r_{\rm max}$	S/N$_{\rm con}$	S/N$_{\rm line}$	RMID	$\tau_{\rm JAV}$ (days)	Fraction Rejected	$r_{\rm max}$	S/N$_{\rm con}$	S/N$_{\rm line}$
531	$157.4^{+18.0}_{-30.8}$	0.71	0.67	7.50	3.40	665	$198.5^{+21.6}_{-68.2}$	0.26	0.78	11.50	1.76
532	$633.1^{+26.9}_{-148.0}$	0.01	0.31	0.00	3.08	670	$-512.8^{+226.3}_{-155.0}$	0.56	0.52	21.00	1.55
533	$239.9^{+26.2}_{-19.8}$	0.59	0.37	7.00	2.56	676	$-600.5^{+170.4}_{-115.6}$	0.64	0.32	14.20	0.00
535	$-597.1^{+19.0}_{-30.9}$	0.32	−0.03	14.20	3.00	678	$179.7^{+46.6}_{-94.7}$	0.00	0.41	13.50	0.84
538	$-422.1^{+51.7}_{-72.4}$	0.31	0.30	11.00	3.94	680	$18.7^{+81.8}_{-68.2}$	0.65	0.47	12.50	1.75
540	$310.0^{+88.6}_{-154.2}$	0.31	0.56	11.00	0.00	682	$648.9^{+12.7}_{-27.9}$	0.10	0.29	13.00	2.64
542	$72.3^{+92.4}_{-82.5}$	0.37	0.42	6.00	1.20	686	$202.6^{+39.4}_{-19.8}$	0.19	0.58	8.00	3.09
543	$161.9^{+93.7}_{-135.1}$	0.19	0.18	9.00	1.21	687	$508.6^{+171.0}_{-149.4}$	0.31	0.45	10.00	1.78
549	$228.9^{+17.4}_{-23.6}$	0.02	0.74	16.00	3.41	688	$-102.1^{+189.9}_{-173.6}$	0.32	0.56	22.00	1.10
550	$463.9^{+36.5}_{-82.2}$	0.02	0.46	8.00	3.04	689	$474.0^{+68.7}_{-126.9}$	0.00	0.58	8.00	3.02
553	$655.5^{+80.2}_{-50.7}$	0.43	0.47	8.00	1.65	690	$144.0^{+40.2}_{-41.9}$	0.31	0.61	16.25	0.71
554	$525.1^{+55.2}_{-33.0}$	0.05	0.59	7.33	2.42	692	$-316.7^{+630.6}_{-307.6}$	0.00	0.45	11.67	0.29
555	$-696.1^{+100.7}_{-14.5}$	0.52	0.49	13.00	3.85	693	$252.5^{+15.2}_{-28.5}$	0.42	0.39	11.00	1.78
556	$-269.7^{+92.7}_{-106.9}$	0.07	0.85	13.50	2.29	695	$249.3^{+90.5}_{-62.7}$	0.43	0.54	7.00	1.82
557	$325.8^{+53.0}_{-69.3}$	0.44	0.66	12.00	0.00	698	$145.0^{+36.8}_{-25.3}$	0.77	0.70	19.00	2.83
560	$582.6^{+14.9}_{-15.0}$	0.25	−0.02	13.00	2.70	699	$240.9^{+25.4}_{-45.2}$	0.03	0.64	13.50	0.00
561	$316.7^{+140.5}_{-91.4}$	0.59	0.44	13.20	1.52	703	$583.6^{+66.3}_{-72.5}$	0.09	0.61	12.00	1.72
562	$597.9^{+68.7}_{-129.2}$	0.40	0.54	9.00	2.01	704	$-567.9^{+61.9}_{-45.4}$	0.57	0.49	14.00	1.48
563	$488.2^{+142.1}_{-51.2}$	0.01	0.34	7.67	2.64	705	$202.0^{+37.7}_{-27.9}$	0.49	0.47	14.67	3.12
564	$602.1^{+104.8}_{-138.9}$	0.23	0.34	10.67	1.04	706	$-68.1^{+26.6}_{-10.4}$	0.45	0.43	14.50	0.49
573	$565.1^{+44.9}_{-180.7}$	0.14	0.29	13.00	2.06	710	$480.5^{+214.5}_{-195.2}$	0.16	0.28	11.00	1.10
574	$652.0^{+37.9}_{-47.8}$	0.21	0.13	7.50	2.68	711	$-663.5^{+110.6}_{-30.8}$	0.53	0.63	12.00	1.98
575	$540.9^{+22.8}_{-35.6}$	0.33	0.37	10.33	4.04	713	$68.4^{+99.5}_{-78.2}$	0.14	0.74	9.00	1.96
578	$429.0^{+140.6}_{-75.7}$	0.12	0.50	14.00	0.70	715	$-602.5^{+14.5}_{-90.9}$	0.59	0.31	8.67	1.28
579	$148.9^{+183.3}_{-13.5}$	0.04	0.50	19.00	2.64	718	$89.9^{+398.9}_{-279.0}$	0.30	0.44	12.00	0.00
583	$249.9^{+16.8}_{-14.8}$	0.48	0.18	15.00	2.70	722	$148.7^{+46.4}_{-46.6}$	0.11	0.52	16.00	4.16
584	$-591.9^{+41.5}_{-89.1}$	0.31	0.18	7.00	2.85	723	$209.3^{+75.6}_{-197.5}$	0.27	0.38	15.50	0.00
585	$65.3^{+65.1}_{-18.8}$	0.05	0.66	14.00	0.67	725	$-1.0^{+8.1}_{-9.7}$	0.46	0.53	8.25	1.56
586	$-69.4^{+48.2}_{-199.7}$	0.16	0.47	10.00	2.80	729	$112.7^{+86.9}_{-57.0}$	0.62	0.66	8.50	0.63
591	$-249.1^{+38.4}_{-45.6}$	0.87	0.35	11.00	0.76	734	$289.9^{+46.1}_{-36.5}$	0.02	0.81	8.50	2.37
594	$192.1^{+31.1}_{-19.9}$	0.04	0.49	11.50	1.97	735	$637.6^{+52.9}_{-111.5}$	0.34	0.39	11.00	2.34
595	$-619.6^{+76.1}_{-27.9}$	0.58	0.16	0.00	0.81	737	$-534.4^{+55.1}_{-109.5}$	0.68	0.22	9.67	0.00
596	$649.1^{+83.8}_{-208.8}$	0.55	0.44	13.00	1.45	738	$146.7^{+11.4}_{-10.6}$	0.29	0.15	11.00	0.95
600	$636.3^{+28.9}_{-54.0}$	0.07	0.08	14.67	2.93	739	$214.1^{+40.9}_{-38.2}$	0.19	0.55	6.00	2.63
602	$-390.8^{+47.2}_{-24.2}$	0.09	0.23	9.00	2.01	743	$191.1^{+67.3}_{-65.8}$	0.12	0.38	4.00	3.78
609	$-189.4^{+9.5}_{-9.2}$	0.79	0.11	13.00	2.13	748	$621.4^{+33.4}_{-86.0}$	0.17	0.33	10.00	2.12
611	$-79.5^{+241.4}_{-196.4}$	0.57	0.41	12.41	0.53	749	$707.2^{+36.9}_{-51.4}$	0.56	0.26	12.00	0.85
612	$715.7^{+14.6}_{-41.9}$	0.56	0.39	6.00	1.56	751	$-690.9^{+47.7}_{-23.5}$	0.80	0.48	12.00	1.93
613	$651.2^{+45.5}_{-42.1}$	0.43	0.44	0.00	2.61	752	$187.8^{+17.4}_{-26.4}$	0.49	0.22	17.00	1.64
614	$92.5^{+99.6}_{-7.2}$	0.53	0.68	10.00	4.90	753	$-102.5^{+52.5}_{-56.6}$	0.22	0.33	9.50	1.60
616	$684.9^{+48.8}_{-113.4}$	0.24	0.35	12.33	0.90	754	$-198.5^{+22.4}_{-36.7}$	0.07	0.79	10.00	2.33
620	$-196.5^{+26.6}_{-28.3}$	0.32	0.23	8.00	2.51	759	$233.2^{+142.1}_{-73.8}$	0.28	0.40	8.00	0.00
621	$358.2^{+44.6}_{-73.9}$	0.30	0.37	14.00	1.29	763	$-181.6^{+15.7}_{-32.0}$	0.33	0.63	10.50	3.41
623	$573.0^{+76.9}_{-134.6}$	0.01	0.60	10.00	0.52	770	$-8.7^{+71.5}_{-135.0}$	0.57	0.32	4.20	0.00
629	$168.5^{+27.2}_{-18.7}$	0.30	0.23	0.00	0.69	771	$363.0^{+80.5}_{-96.2}$	0.14	0.58	13.38	0.00
630	$163.0^{+217.7}_{-186.5}$	0.54	0.27	7.33	0.46	774	$86.6^{+39.7}_{-51.2}$	0.00	0.79	15.60	1.14
631	$-683.1^{+82.2}_{-55.1}$	0.02	0.74	15.00	0.00	777	$260.2^{+51.5}_{-61.6}$	0.65	0.32	10.75	0.00
633	$220.5^{+110.3}_{-29.4}$	0.67	0.57	8.50	1.69	784	$-4.0^{+38.5}_{-25.7}$	0.04	0.62	5.10	0.00
635	$592.5^{+73.7}_{-89.3}$	0.13	0.43	13.00	2.62	794	$-606.9^{+29.2}_{-5.0}$	0.57	0.06	7.00	1.74
636	$95.8^{+70.6}_{-146.9}$	0.33	0.55	8.00	0.00	796	$-375.6^{+151.8}_{-65.1}$	0.19	0.39	6.00	0.00
646	$640.5^{+13.3}_{-39.9}$	0.14	0.09	8.00	0.00	801	$601.1^{+29.5}_{-35.6}$	0.11	0.01	9.00	3.85
647	$273.9^{+93.2}_{-186.6}$	0.12	0.33	26.00	0.73	803	$203.1^{+34.1}_{-34.9}$	0.01	0.70	6.00	1.62
648	$557.7^{+19.5}_{-72.8}$	0.13	0.31	7.00	2.58	809	$290.1^{+73.9}_{-135.3}$	0.42	0.62	9.00	2.36
651	$196.9^{+21.5}_{-38.5}$	0.51	0.76	12.67	3.53	810	$-351.0^{+51.6}_{-67.6}$	0.58	0.40	11.00	0.33
658	$139.8^{+102.5}_{-24.0}$	0.43	0.56	7.00	1.50	811	$-219.2^{+46.0}_{-33.6}$	0.39	0.38	10.00	0.80
660	$54.6^{+67.8}_{-41.0}$	0.26	0.60	11.67	0.21	816	$168.8^{+23.3}_{-25.9}$	0.29	0.34	11.00	1.32
661	$479.6^{+63.6}_{-42.0}$	0.23	0.22	13.00	1.65	818	$219.4^{+16.8}_{-29.2}$	0.17	0.30	17.60	2.42

Table 5
(Continued)

RMID	τ_{JAV} (days)	Fraction Rejected	r_{max}	S/N$_{con}$	S/N$_{line}$
820	$647.9^{+53.5}_{-95.6}$	0.17	0.54	11.00	0.00
821	$736.8^{+9.7}_{-28.5}$	0.65	0.69	13.00	1.57
827	$408.4^{+54.4}_{-57.6}$	0.26	0.91	14.00	3.08
828	$311.1^{+21.5}_{-22.7}$	0.43	0.32	14.00	0.95
829	$159.3^{+48.8}_{-55.1}$	0.06	0.46	5.00	3.00
831	$-605.8^{+72.3}_{-86.9}$	0.43	0.56	11.80	3.10
835	$475.6^{+85.5}_{-32.5}$	0.32	0.46	10.00	0.19

(This table is available in machine-readable form.)

ORCID iDs

C. J. Grier https://orcid.org/0000-0001-9920-6057
Yue Shen https://orcid.org/0000-0003-1659-7035
Keith Horne https://orcid.org/0000-0003-1728-0304
W. N. Brandt https://orcid.org/0000-0002-0167-2453
J. R. Trump https://orcid.org/0000-0002-1410-0470
P. B. Hall https://orcid.org/0000-0002-1763-5825
K. Kinemuchi https://orcid.org/0000-0001-7908-7724
Luis C. Ho https://orcid.org/0000-0001-6947-5846
Y. Homayouni https://orcid.org/0000-0002-0957-7151
Jennifer I-Hsiu Li https://orcid.org/0000-0002-0311-2812
Ian D. McGreer https://orcid.org/0000-0002-3461-5228
B. M. Peterson https://orcid.org/0000-0001-6481-5397
Dmitry Bizyaev https://orcid.org/0000-0002-3601-133X
K. S. Dawson https://orcid.org/0000-0002-0553-3805
Siyao Jia https://orcid.org/0000-0001-5341-0765
Linhua Jiang https://orcid.org/0000-0003-4176-6486
Kaike Pan https://orcid.org/0000-0002-2835-2556
Kara A. Ponder https://orcid.org/0000-0002-8207-3304
Jesse Rogerson https://orcid.org/0000-0002-7078-1776
Tianmeng Zhang https://orcid.org/0000-0002-8531-5161
Hu Zou https://orcid.org/0000-0002-6684-3997

References

Ahn, C. P., Alexandroff, R., Allende Prieto, C., et al. 2014, ApJS, 211, 17
Akritas, M. G., & Bershady, M. A. 1996, ApJ, 470, 706
Alard, C. 2000, A&AS, 144, 363
Alard, C., & Lupton, R. H. 1998, ApJ, 503, 325
Alexander, T. 1997, in Astronomical Time Series, ed. D. Maoz, A. Sternberg, & E. M. Leibowitz (Dordrecht: Kluwer), 163
Assef, R. J., Denney, K. D., Kochanek, C. S., et al. 2011, ApJ, 742, 93
Aune, S., Boulade, O., Charlot, X., et al. 2003, Proc. SPIE, 4841, 513
Barlow, T. A. 1993, PhD thesis, California Univ.
Barth, A. J., Bennert, V. N., Canalizo, G., et al. 2015, ApJS, 217, 26
Baskin, A., & Laor, A. 2005, MNRAS, 356, 1029
Bentz, M. C., Denney, K. D., Grier, C. J., et al. 2013, ApJ, 767, 149
Bentz, M. C., & Katz, S. 2015, PASP, 127, 67
Bentz, M. C., Walsh, J. L., Barth, A. J., et al. 2009, ApJ, 705, 199
Bentz, M. C., Walsh, J. L., Barth, A. J., et al. 2010, ApJ, 716, 993
Blandford, R. D., & McKee, C. F. 1982, ApJ, 255, 419
Blanton, M. R., Bershady, M. A., Abolfathi, B., et al. 2017, AJ, 154, 28
Brotherton, M. S., Runnoe, J. C., Shang, Z., & DiPompeo, M. A. 2015, MNRAS, 451, 1290
Capellupo, D. M., Hamann, F., Shields, J. C., Rodríguez Hidalgo, P., & Barlow, T. A. 2011, MNRAS, 413, 908
Clavel, J., Wamsteker, W., & Glass, I. S. 1989, ApJ, 337, 236
Coatman, L., Hewett, P. C., Banerji, M., et al. 2017, MNRAS, 465, 2120
Dawson, K. S., Kneib, J.-P., Percival, W. J., et al. 2016, AJ, 151, 44
Dawson, K. S., Schlegel, D. J., Ahn, C. P., et al. 2013, AJ, 145, 10

De Rosa, G., Peterson, B. M., Ely, J., et al. 2015, ApJ, 806, 128
Denney, K. D. 2012, ApJ, 759, 44
Denney, K. D., Horne, K., Brandt, W. N., et al. 2016a, ApJ, 833, 33
Denney, K. D., Horne, K., Shen, Y., et al. 2016b, ApJS, 224, 14
Denney, K. D., Peterson, B. M., Pogge, R. W., et al. 2010, ApJ, 721, 715
Doi, M., Tanaka, M., Fukugita, M., et al. 2010, AJ, 139, 1628
Du, P., Hu, C., Lu, K.-X., et al. 2014, ApJ, 782, 45
Du, P., Lu, K.-X., Hu, C., et al. 2016a, ApJ, 820, 27
Du, P., Lu, K.-X., Zhang, Z.-X., et al. 2016b, ApJ, 825, 126
Edelson, R., Gelbord, J., Cackett, E., et al. 2019, ApJ, 870, 123
Edelson, R. A., & Krolik, J. H. 1988, ApJ, 333, 646
Eisenstein, D. J., Weinberg, D. H., Agol, E., et al. 2011, AJ, 142, 72
Fausnaugh, M. M., Denney, K. D., Barth, A. J., et al. 2016, ApJ, 821, 56
Fausnaugh, M. M., Grier, C. J., Bentz, M. C., et al. 2017, ApJ, 840, 97
Ferrarese, L., & Merritt, D. 2000, ApJL, 539, L9
Filiz Ak, N., Brandt, W. N., Hall, P. B., et al. 2013, ApJ, 777, 168
Filiz Ak, N., Brandt, W. N., Hall, P. B., et al. 2014, ApJ, 791, 88
Fonseca Alavarez, G., Trump, J. R., & Homayouni, Y. 2019, arXiv:1910.10719
Fukugita, M., Ichikawa, T., Gunn, J. E., et al. 1996, AJ, 111, 1748
Gaskell, C. M. 1982, ApJ, 263, 79
Gaskell, C. M., & Sparke, L. S. 1986, ApJ, 305, 175
Gebhardt, K., Bender, R., Bower, G., et al. 2000, ApJL, 539, L13
Gravity Collaboration, Sturm, E., Dexter, J., et al. 2018, Natur, 563, 657
Grier, C. J., Hall, P. B., Brandt, W. N., et al. 2015, ApJ, 806, 111
Grier, C. J., Peterson, B. M., Bentz, M. C., et al. 2008, ApJ, 688, 837
Grier, C. J., Peterson, B. M., Pogge, R. W., et al. 2012, ApJ, 755, 60
Grier, C. J., Trump, J. R., Shen, Y., et al. 2017, ApJ, 851, 21
Gültekin, K., Richstone, D. O., Gebhardt, K., et al. 2009, ApJ, 698, 198
Gunn, J. E., Siegmund, W. A., Mannery, E. J., et al. 2006, AJ, 131, 2332
Hemler, Z. S., Grier, C. J., Brandt, W. N., et al. 2019, ApJ, 872, 21
Homayouni, Y., Trump, J. R., Grier, C. J., et al. 2019, ApJ, 880, 126
Hoormann, J. K., Martini, P., Davis, T. M., et al. 2019, MNRAS, 487, 3650
Hu, C., Du, P., Lu, K.-X., et al. 2015, ApJ, 804, 138
Kaspi, S., Brandt, W. N., Maoz, D., et al. 2007, ApJ, 659, 997
Kaspi, S., Maoz, D., Netzer, H., et al. 2005, ApJ, 629, 61
Kaspi, S., Smith, P. S., Netzer, H., et al. 2000, ApJ, 533, 631
Kelly, B. C. 2007, ApJ, 665, 1489
Kelly, B. C., Bechtold, J., & Siemiginowska, A. 2009, ApJ, 698, 895
King, A. L., Martini, P., Davis, T. M., et al. 2015, MNRAS, 453, 1701
Kollmeier, J. A., Zasowski, G., Rix, H.-W., et al. 2017, arXiv:1711.03234
Koratkar, A. P., & Gaskell, C. M. 1989, ApJ, 345, 637
Koratkar, A. P., & Gaskell, C. M. 1991, ApJS, 75, 719
Korista, K. T., Alloin, D., Barr, P., et al. 1995, ApJS, 97, 285
Kormendy, J., & Richstone, D. 1995, ARA&A, 33, 581
Kozłowski, S. 2016, MNRAS, 459, 2787
Kozłowski, S. 2017, A&A, 597, 128
Kozłowski, S., Kochanek, C. S., Udalski, A., et al. 2010, ApJ, 708, 927
Li, J., Shen, Y., Brandt, W. N., et al. 2019, ApJ, 884, 119
Lira, P., Kaspi, S., Netzer, H., et al. 2018, ApJ, 865, 56
Lundgren, B. F., Wilhite, B. C., Brunner, R. J., et al. 2007, ApJ, 656, 73
MacLeod, C. L., Ivezić, Ž., Kochanek, C. S., et al. 2010, ApJ, 721, 1014
MacLeod, C. L., Ivezić, Ž., Sesar, B., et al. 2012, ApJ, 753, 106
Magorrian, J., Tremaine, S., Richstone, D., et al. 1998, AJ, 115, 2285
Maronna, R. A., Martin, R. D., & Yohai, V. J. 2006, Robust Statistics (New York: Wiley)
Matsuoka, Y., Strauss, M. A., Shen, Y., et al. 2015, ApJ, 811, 91
McConnachie, A., Babusiaux, C., Balogh, M., et al. 2016, arXiv:1606.00043
McConnell, N. J., & Ma, C.-P. 2013, ApJ, 764, 184
Morgan, C. W., Kochanek, C. S., Morgan, N. D., & Falco, E. E. 2010, ApJ, 712, 1129
Mosquera, A. M., Kochanek, C. S., Chen, B., et al. 2013, ApJ, 769, 53
Nemmen, R. S., Georganopoulos, M., Guiriec, S., et al. 2012, Sci, 338, 1445
Netzer, H., Lira, P., Trakhtenbrot, B., Shemmer, O., & Cury, I. 2007, ApJ, 671, 1256
O'Brien, P. T., Dietrich, M., Leighly, K., et al. 1998, ApJ, 509, 163
Peterson, B. M. 1993, PASP, 105, 247
Peterson, B. M. 2011, Narrow-Line Seyfert 1 Galaxies and their Place in the Universe Masses, Host Galaxies, Evolution (Trieste: SISSA)
Peterson, B. M., Bentz, M. C., Desroches, L., et al. 2005, ApJ, 632, 799
Peterson, B. M., Denney, K. D., De Rosa, G., et al. 2013, ApJ, 779, 109
Peterson, B. M., Ferrarese, L., Gilbert, K. M., et al. 2004, ApJ, 613, 682
Peterson, B. M., Wanders, I., Bertram, R., et al. 1998, ApJ, 501, 82
Reichert, G. A., Rodriguez-Pascual, P.M., Alloin, D., et al. 1994, ApJ, 425, 582
Richards, G. T., Kruczek, N. E., Gallagher, S. C., et al. 2011, AJ, 141, 167
Richards, G. T., Lacy, M., Storrie-Lombardi, L. J., et al. 2006, ApJS, 166, 470

Rodriguez-Pascual, P. M., Alloin, D., Clavel, J., et al. 1997, ApJS, 110, 9
Runnoe, J. C., Brotherton, M. S., Shang, Z., & DiPompeo, M. A. 2013, MNRAS, 434, 848
Shang, Z., Wills, B. J., Wills, D., & Brotherton, M. S. 2007, AJ, 134, 294
Shen, Y. 2013, BASI, 41, 61
Shen, Y., Brandt, W. N., Dawson, K. S., et al. 2015a, ApJS, 216, 4
Shen, Y., Greene, J. E., Ho, L. C., et al. 2015b, ApJ, 805, 96
Shen, Y., Grier, C. J., Horne, K., et al. 2019a, ApJL, 883, L14
Shen, Y., Hall, P. B., Horne, K., et al. 2019b, ApJS, 241, 34
Shen, Y., Horne, K., Grier, C. J., et al. 2016, ApJ, 818, 30
Shen, Y., & Kelly, B. C. 2012, ApJ, 746, 169
Shen, Y., Richards, G. T., Strauss, M. A., et al. 2011, ApJS, 194, 45
Smee, S. A., Gunn, J. E., Uomoto, A., et al. 2013, AJ, 146, 32
Starkey, D. A., Horne, K., & Villforth, C. 2016, MNRAS, 456, 1960
Sun, M., Grier, C. J., & Peterson, B. M. 2018, PyCCF: Python Cross Correlation Function for Reverberation Mapping Studies, Astrophysics Source Code Library, ascl:1805.032
Sun, M., Trump, J. R., Shen, Y., et al. 2015, ApJ, 811, 42
Swann, E., Sullivan, M., Carrick, J., et al. 2019, arXiv:1903.02476
Trakhtenbrot, B., & Netzer, H. 2012, MNRAS, 427, 3081
Trevese, D., Perna, M., Vagnetti, F., Saturni, F. G., & Dadina, M. 2014, ApJ, 795, 164
Vestergaard, M., & Peterson, B. M. 2006, ApJ, 641, 689
Wanders, I., Peterson, B. M., Alloin, D., et al. 1997, ApJS, 113, 69
Wang, S., Shen, Y., Horne, K., et al. 2019, ApJ, 882, 4
Wang, T., Yang, C., Wang, H., & Ferland, G. 2015, ApJ, 814, 150
White, R. J., & Peterson, B. M. 1994, PASP, 106, 879
Williams, G. G., Olszewski, E., Lesser, M. P., & Burge, J. H. 2004, Proc. SPIE, 5492, 787
Woo, J.-H., Yoon, Y., Park, S., Park, D., & Kim, S. C. 2015, ApJ, 801, 38
Yu, Z., Kochanek, C. S., Peterson, B. M., et al. 2019, arXiv:1909.03072
Yue, M., Jiang, L., Shen, Y., et al. 2018, ApJ, 863, 21
Zu, Y., Kochanek, C. S., Kozłowski, S., & Udalski, A. 2013, ApJ, 765, 106
Zu, Y., Kochanek, C. S., & Peterson, B. M. 2011, ApJ, 735, 80